PHYSICAL REVIEW E **78**, 066201 (2008)

Dynamics of two laterally coupled semiconductor lasers: Strong- and weak-coupling theory

H. Erzgräber and S. Wieczorek
School of Engineering, Computing and Mathematics, University of Exeter, Exeter EX4 4QF, United Kingdom

B. Krauskopf
Department of Engineering Mathematics, University of Bristol, Bristol BS8 1TR, United Kingdom

(Received 4 August 2008; revised manuscript received 17 September 2008; published 1 December 2008)

The stability and nonlinear dynamics of two semiconductor lasers coupled side to side via evanescent waves are investigated by using three different models. In the composite-cavity model, the coupling between the lasers is accurately taken into account by calculating electric field profiles (composite-cavity modes) of the whole coupled-laser system. A bifurcation analysis of the composite-cavity model uncovers how different types of dynamics, including stationary phase-locking, periodic, quasiperiodic, and chaotic intensity oscillations, are organized. In the individual-laser model, the coupling between individual lasers is introduced phenomenologically with *ad hoc* coupling terms. Comparison with the composite-cavity model reveals drastic differences in the dynamics. To identify the causes of these differences, we derive a coupled-laser model with coupling terms which are consistent with the solution of the wave equation and the relevant boundary conditions. This coupled-laser model reproduces the dynamics of the composite-cavity model under weak-coupling conditions.

DOI: 10.1103/PhysRevE.78.066201 PACS number(s): 05.45.Gg, 02.30.Ks, 02.30.Oz

I. INTRODUCTION

Understanding the dynamical complexity of laser systems has been a focus of numerous studies since the first realization of lasers. Even very early studies developed the idea of coupling a laser either to the environment in general or, more specifically, to another laser; see Refs. [1–3]. Recent developments make it feasible to manufacture sophisticated (semiconductor) laser devices with many different active and passive sections. From the application point of view, there is a strong desire to employ coupled-laser structures, for example, as high-power laser sources or as high-frequency optical clocks [4,5]. From the fundamental point of view, coupled lasers became an attractive choice for the study of synchronization properties of coupled oscillators more generally; see, for example, Refs. [6–11]. This paper focuses on three selected models to provide further understanding of the key model components and the resulting instabilities in coupled-laser systems.

Different models of coupled-laser systems emerged from different concepts of obtaining (approximate) solutions to the wave equation governing the spatiotemporal dynamics of the laser field. They include low-dimensional rate equations, which are ordinary differential equations [12–16], rate equations with time-delayed coupling [17–19], composite-cavity models [5,20–22], supermode models [23], and partial differential equation models, such as traveling-wave models [24–27]. Because of their simplicity, low-dimensional rate equation models are an attractive choice for the analysis of the stability and nonlinear dynamical behavior with tools from bifurcation theory. However, these models neglect coupling effects in the space dependence of the electric field and are unsuitable for describing strongly coupled lasers. Partial differential equation models, on the other hand, are potentially very accurate but, due to their infinite-dimensional nature, they do not lend themselves easily to (comprehensive and global) stability analysis. Composite-cavity models strike a good compromise between accuracy and suitability for stability analysis. Physically, a composite-cavity model takes into account the space dependence of the electric field and is, hence, valid for arbitrary coupling strengths. Mathematically, a composite-cavity model consists of a set of ordinary differential equations governing the time evolution of the complex composite-mode amplitudes, in conjunction with a set of algebraic constraints that determine the spatial mode profiles. Most importantly, the stability and dynamics of this type of model can still be analyzed with numerical continuation techniques.

Although current research moves toward complicated laser structures with various coupling conditions, such as two-dimensional arrays [28–32] and photonic crystal laser arrays [33,34], there are important aspects of modeling and nonlinear dynamics of two-laser systems that have not been fully understood. Here, we address two specific questions to provide a better understanding of two-laser systems. Our results are also important for the study of nonlinear dynamics of multilaser systems.

The first question addresses the key aspects of nonlinear dynamics in two side-to-side coupled lasers. Specifically, we adapt the *composite-cavity model* devised in Refs. [21,35] to describe a concrete laser device consisting of two side-to-side coupled semiconductor lasers. We provide a comprehensive bifurcation analysis of stationary phase-locking, periodic, quasiperiodic, and chaotic intensity oscillations in this model. Bifurcation diagrams for representative values of the linewidth-enhancement factor are presented in the plane of the distance between the lasers (which accounts for the coupling strength) and the laser-width difference (which introduces frequency detuning between the lasers). In particular, we identify interesting differences in dynamical behavior under strong- and weak-coupling conditions. The bifurcation diagrams serve as a benchmark, against which simpler models can be compared. Furthermore, they provide a valuable link between the specific configuration parameters of a real laser device and the dimensionless coupling parameters found in the simpler models. The results obtained for two

side-to-side coupled lasers are then compared with a similar study of the composite-cavity model for two face-to-face coupled lasers [20,36,37].

Second, we consider whether there is a simple rate equation model that can reproduce the dynamics of the more accurate composite-cavity model, at least when the coupling is not too strong. This question becomes relevant in studying general properties of multilaser arrays where simple yet adequate models are strongly desired. We first analyze a widely-used rate equation model [13,38–45], which we refer to as an *individual-laser model*, and uncover dynamics that is significantly different from those found in the composite-cavity model. Rather surprisingly, in the individual-laser model the laser's intensity diverges off to infinity already at weak-coupling conditions. We show that the discrepancies arise because in the individual-laser model the coupling terms which are introduced phenomenologically are not in agreement with the boundary conditions of the coupled-laser system. Specifically, we use an approach similar to that in Ref. [2] to derive simple rate equations for side-to-side coupled lasers, which we refer to as the *coupled-laser model*. Our calculations give coupling terms that are consistent with the solution of the wave equation and appropriate boundary conditions. Furthermore, they reproduce the complicated dynamical behavior of the more accurate composite cavity model, provided the coupling is not too strong.

This paper is structured as follows. Section II describes the geometry of the side-to-side coupled-laser device. In Sec. III we present the composite-cavity model of this coupled-laser device. Spatial composite-cavity mode profiles are calculated as solutions of the inhomogeneous wave equation in Sec. III A. Temporal dynamics of the composite-cavity modes are discussed in Sec. III B with two-dimensional bifurcation diagrams in the plane of the half distance between the lasers and the laser-width difference. In Sec. IV we consider simpler rate equation models of coupled lasers. After showing significant differences in the dynamics of the individual-laser model and the composite-cavity model, we derive a coupled-laser model that takes into account the proper boundary conditions of the coupled-laser system. We summarize our results in Sec. V. Appendixes contain details about the scaling of the model equations and an alternative representation in polar coordinates for convenience.

II. TWIN-STRIPE LASER

While the focus of this paper is on the robust aspects of coupled-laser dynamics that do not depend on details of the laser design, composite-cavity theory requires an example of a specific laser configuration. Therefore, we choose to model a laser device that is known as a twin-stripe laser; it is depicted in Fig. 1. The two active regions A and B are oriented along the longitudinal z direction in which the laser beam propagates. They are coupled via the evanescent field in the lateral x direction. The stripes have refractive indices n_A and n_B, respectively. The stripes have widths w_A and w_B in the x direction, and they are at distance d from the origin of the x direction, which is chosen in the middle between the two stripes for convenience. The passive region with refractive

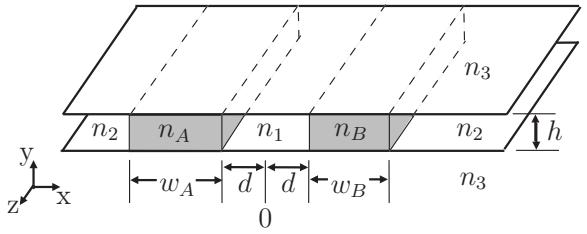

FIG. 1. Sketch of the twin stripe laser geometry with two stripes of thickness h, widths w_A and w_B, and the distance $2d$. n_A, n_B,n_1, n_2, and n_3 denote different refractive indices.

index $n_1 < n_A, n_B$ between the stripes is of width $2d$, and we refer to d as the half distance between the stripes. Furthermore, each stripe has thickness h and light is confined in the y direction by passive layers of semiconductor material with refractive index $n_3 < n_1, n_2, n_A, n_B$. For calculations, we use the realistic values $n_A = n_B = 3.61$, $n_1 = n_2 = 3.6$, $w_A \approx w_B \approx 4$ μm, $0 < d < 4$ μm, and $h = 0.05$ μm. The twin stripe laser has attracted considerable attention during the past years, as a device in which to study fundamental aspects of coupled nonlinear oscillators, but also for possible technological applications [46–55].

III. STRONG-COUPLING THEORY

In semiclassical laser theory, the spatiotemporal dynamics of the laser field is described by the wave equation

$$-\nabla^2 \mathcal{E}(\vec{r},t) + \mu_0 \sigma \frac{\partial \mathcal{E}(\vec{r},t)}{\partial t} + \mu_0 \epsilon_0 \mathrm{n}^2(\vec{r}) \frac{\partial^2 \mathcal{E}(\vec{r},t)}{\partial^2 t} = -\mu_0 \frac{\partial^2 \mathcal{P}(\vec{r},t)}{\partial^2 t}, \tag{1}$$

where $\mathcal{E}(\vec{r},t)$ is the electric field in the laser and $\mathcal{P}(\vec{r},t)$ is the macroscopic polarization. The macroscopic polarization arises from microscopic dipoles induced by the assumed electric field according to the laws of quantum mechanics. Also, it acts as a source in Eq. (1) giving rise to the reaction electric field. Equation (1) is combined with a suitable quantum mechanical description of the active medium, under the assumption that the assumed electric field inducing polarization equals the reaction field. Such a formalism gives a self-consistent description of the spatiotemporal laser dynamics; see Ref. [56], p. 98.

The inhomogenous wave equation (1) is solved by expanding the electric field in terms of solutions to the homogeneous wave equation, that is, Eq. (1) with $\mathcal{P}(\vec{r},t) = 0$. These solutions are denoted $U_a(\vec{r})$, where a refers to the index triple $a = (j,l,m)$ for the three spatial dimensions. We write

$$\mathcal{E}(\vec{r},t) = \frac{1}{2} \sum_a |E_a(t)| e^{-i[\nu_a t + \Phi_a(t)]} U_a(\vec{r}) + \text{c.c.},$$

$$\mathcal{P}(\vec{r},t) = \frac{1}{2} \sum_a P_a(t) e^{-i[\nu_a t + \Phi_a(t)]} U_a(\vec{r}) + \text{c.c.}, \tag{2}$$

where $|E_a(t)|$ is the slowly varying amplitude of mode a, $\Phi_a(t)$ is the slowly varying phase, ν_a is some conveniently

chosen reference frequency, and c.c. stands for the complex conjugate. In complex form the slowly varying field reads

$$E_a(t) = |E_a(t)|\exp[-i\Phi_a(t)].$$

In the composite-cavity mode approach, when solving the homogeneous wave equation (or the Helmholz equation)

$$\left(\vec{\nabla}^2 + n^2(\vec{r})\frac{\Omega_a^2}{c^2}\right)U_a(\vec{r}) = 0, \tag{3}$$

one uses the refractive index $n(\vec{r})$ which describes spatial variations of the entire multilaser structure [22]. The resulting $U_a(\vec{r})$, which form the basis of the modal decomposition in Eq. (2), are the eigenmodes of the entire coupled-laser system and, hence, are called the composite-cavity modes. It can be shown that all solutions $U_a(\vec{r})$ of the Helmholz equation (3) satisfy the orthogonality relation

$$\int_{-\infty}^{\infty} d\vec{r}\, n^2(\vec{r})U_a(\vec{r})U_{a'}(\vec{r}) = \mathcal{N}\delta_{aa'}, \tag{4}$$

where $\delta_{aa'}$ is the Kronecker δ. We choose the normalization constant

$$\mathcal{N} = n_b^2(d_0 + w_0)hL,$$

with n_b=3.6, d_0=2 μm, and w_0=4 μm.

Inserting the modal expansion Eqs. (2) into the wave equation (1), using Eq. (4) and the slowly varying amplitude and phase approximation [neglecting terms containing $\ddot{E}_a(t)$, $\ddot{\Phi}_a(t)$, $\ddot{P}_a(t)$, $\dot{E}_a(t)\dot{\Phi}_a(t)$, $\sigma\dot{E}_a(t)$, $\sigma\dot{\Phi}_a(t)$, $\dot{\Phi}_a(t)\dot{P}_a(t)$, $\dot{\Phi}_a(t)P_a(t)$, and $\dot{P}_a(t)$], and assuming $\Omega_a^2 - [\nu_a + \dot{\Phi}_a(t)]^2 \approx 2\nu_a[\Omega_a - \nu_a - \dot{\Phi}_a(t)]$ (see Ref. [56], p. 100 or [57]), we obtain the so-called self-consistency equations. They form a set of ordinary differential equations for the slowly varying amplitude and phase of the composite-cavity mode a:

$$\frac{d|E_a(t)|}{dt} = -\frac{\sigma}{2\epsilon_0}|E_a(t)| - \sum_{a'}\frac{\nu_{a'}}{2\epsilon_0 n_b^2}\mathrm{Im}[P_{a'}(t)]\Delta_{aa'}, \tag{5}$$

$$\frac{d\Phi_a(t)}{dt} = (\Omega_a - \nu_a) - \sum_{a'}\frac{\nu_{a'}}{2\epsilon_0 n_b^2}\frac{\mathrm{Re}[P_{a'}(t)]}{|E_a(t)|}\Delta_{aa'}, \tag{6}$$

where $\Delta_{aa'}$ are the modal integrals

$$\Delta_{aa'} = \frac{n_b^2}{\mathcal{N}}\int_{-\infty}^{\infty} d\vec{r}\, U_a(\vec{r})U_{a'}(\vec{r}). \tag{7}$$

The coupled-laser geometry determines the composite-cavity mode frequencies Ω_a and the number of polarization modes coupled to a single mode of the electric field. For many laser structures such as the one considered here, one can approximate

$$\Delta_{a,a'} \approx \delta_{a,a'}, \tag{8}$$

as we will show in Fig. 3. Then, each mode of the electric field is coupled to just one mode of polarization and the self-consistency Equations (5) and (6) simplify to the commonly known form (see Ref. [56], p. 100):

$$\frac{d|E_a(t)|}{dt} = -\frac{\sigma}{2\epsilon_0}|E_a(t)| - \frac{\nu_a}{2\epsilon_0}\mathrm{Im}[P_a(t)], \tag{9}$$

$$\frac{d\Phi_a(t)}{dt} = (\Omega_a - \nu_a) - \frac{\nu_a}{2\epsilon_0}\frac{\mathrm{Re}[P_a(t)]}{|E_a(t)|}. \tag{10}$$

In order to determine the temporal dynamics of the optical field described by Eqs. (9) and (10) we need to specify an appropriate model for the response of the active medium to a multimode electric field. Specifically, we assume the spatial distribution of carrier density,

$$D(\vec{r},t) = \begin{cases} N_{A,B}(t) & \text{inside stripe } A,B, \\ 0 & \text{elsewhere.} \end{cases} \tag{11}$$

For the given carrier density distribution, the time evolution of $\mathcal{P}(\vec{r},t)$ is derived from quantum mechanics [58]. In semiconductor lasers (which are class-B lasers), the active medium polarization decays much faster than the electric field and the carrier density. Therefore, one can obtain an algebraic equation for each polarization mode:

$$P_a(t) = -\frac{2\epsilon_0 n_b^2}{\nu_a}\sum_{a'}\left(i\frac{c}{n_b}g_{aa'} - \frac{\nu_a}{n_b}\delta n_{aa'}\right)E_{a'}(t). \tag{12}$$

Here, $g_{aa'}$ and $\delta n_{aa'}$ are the modal gain and carrier-induced refractive-index change, respectively, that are associated with the polarization mode a. From the spatial dependence of the carrier density $D(\vec{r},t)$ in Eq. (11) one can see that each polarization mode, or $g_{aa'}$ and $\delta n_{aa'}$, has its source in two active regions [20] so that

$$g_{aa'} = g_{aa'}^A + g_{aa'}^B = g^A(N_A)\mathcal{K}_{aa'}^A + g^B(N_B)\mathcal{K}_{aa'}^B, \tag{13}$$

$$\delta n_{aa'} = \delta n_{aa'}^A + \delta n_{aa'}^B = \delta n_A(N_A)\mathcal{K}_{aa'}^A + \delta n_B(N_B)\mathcal{K}_{aa'}^B. \tag{14}$$

While the local gain $g^{A,B}$ and index change $\delta n^{A,B}$ reflect the local properties of the active media, the spatial mode integrals taken over the active region A,B,

$$\mathcal{K}_{aa'}^{A,B} = \frac{\int_{A,B} d\vec{r}\, n^2(\vec{r})U_a(\vec{r})U_{a'}(\vec{r})}{\mathcal{N}}, \tag{15}$$

depend on the geometry of the coupled-laser system. Specifically, the diagonal terms describe the overlap of the composity-cavity mode with the active region and the off-diagonal terms describe the coupling between different composite-cavity modes.

For semiconductor lasers, g and δn can be approximated by

$$g^{A,B}(N_{A,B}) = g_{\mathrm{thr}} + \xi(N_{A,B} - N_{\mathrm{thr}}),$$

$$\delta n^{A,B}(N_{A,B}) = -\frac{c}{\nu}\alpha N_{A,B}, \tag{16}$$

where we neglect their spectral dependence and assume that the threshold gain g_{thr}, threshold carrier density N_{thr}, differ-

ential gain coefficient ξ, and linewidth enhancement factor α are identical for both lasers. Formulas for g_{thr} and N_{thr} are given in Appendix A.

Finally, the carrier density within each laser evolves as

$$\frac{dN_{A,B}(t)}{dt} = \Lambda_{A,B} - \gamma_N N_{A,B}(t) - \sum_{a,a'} \frac{c\epsilon_0 n_b g_{aa'}^{A,B}}{\hbar \nu_n} |E_a(t)| \times |E_{a'}(t)| \cos(\Phi_{aa'}), \tag{17}$$

where $\Lambda_{A,B}$ is the pump rate in lasers A, and B, γ_N is the carrier decay rate, and $\Phi_{aa'}=\Phi_a-\Phi_{a'}$. See, for example, Refs. [20,37].

In the composite-cavity approach, solutions to the space- and time-dependent parts of Eq. (1) are separated in the following way. The first step requires solution of the spatial mode problem Eq. (3) for the given coupled-laser geometry, for example, face-to-face (see Refs. [20,36,37]) or side-to-side (see Refs. [35,59]) coupling. The second step combines the quantum mechanical description of the active medium and the calculated composite-cavity modes to derive the macroscopic polarization and carrier density equations. Finally, by requiring self-consistency, the dynamics of the laser is determined by Eqs. (5), (6), and (17) which are coupled to the spatial-mode problem Eq. (3) via the modal integrals Eq. (15).

A. Passive composite-cavity modes

The composite-cavity modes are obtained from the Helmholz equation (3) and the appropriate boundary conditions. By assuming that a composite-cavity mode can be factorized as

$$U(\vec{r}) = X(x)Y(y)Z(z),$$

Eq. (3) is separated into three different equations for the x, y, and z directions. Henceforth, we assume a standing-wave solution in the z direction and focus on the x direction only ([35], p. 270):

$$\left(\frac{\partial^2 X}{\partial x^2} + n^2(x)k^2 - k_z^2\right) X(x) = 0. \tag{18}$$

Here, $k_z=5\pi\times 10^6$ m^{-1} is the z component of the total wave vector of magnitude $k=\sqrt{k_x^2+k_y^2+k_z^2}$ and $n(x)$ reflects the refractive index variation in the x direction; see Fig. 1. Furthermore, the electric field and its first derivative have to be continuous at each boundary:

$$\begin{aligned}
&X(-d_A^-) - X(-d_A^+) = 0,\\
&\frac{d}{dx}X(-d_A^-) - \frac{d}{dx}X(-d_A^+) = 0,\\
&X(-d^-) - X(-d^+) = 0,\\
&\frac{d}{dx}X(-d^-) - \frac{d}{dx}X(-d^+) = 0,\\
&X(d^-) - X(d^+) = 0,\\
&\frac{d}{dx}X(d^-) - \frac{d}{dx}X(d^+) = 0,\\
&X(d_B^-) - X(d_B^+) = 0,\\
&\frac{d}{dx}X(d_B^-) - \frac{d}{dx}X(d_B^+) = 0,
\end{aligned} \tag{19}$$

where $d_{A,B}=d+w_{A,B}$. We seek solutions to the boundary value problem Eqs. (18) and (19) in the form

$$X(x) = \begin{cases} G\exp[p_2(x+d+w_A)] & \text{if } x \leqslant -d-w_A,\\ A\sin[p_A(x+d_A)] + B\cos[p_A(x+d_A)] & \text{if } -d-w_A < x \leqslant -d,\\ C\exp[-p_1(x+d)] + D\exp[p_1(x-d)] & \text{if } -d < x \leqslant d,\\ E\sin[p_B(x-d)] + F\cos[p_B(x-d)] & \text{if } d < x \leqslant d+w_B,\\ H\exp[-p_2(x-d_B)] & \text{if } d+w_B \leqslant x. \end{cases} \tag{20}$$

By inserting Eq. (20) into Eq. (18) we obtain equations for the propagation constants p_1, p_2, p_A, p_B:

$$\begin{aligned}
&p_2^2 + n_2^2k^2 - k_z^2 = 0,\\
&-p_A^2 + n_A^2k^2 - k_z^2 = 0,\\
&p_1^2 + n_1^2k^2 - k_z^2 = 0,\\
&-p_B^2 + n_B^2k^2 - k_z^2 = 0.
\end{aligned} \tag{21}$$

The composite-cavity mode amplitudes A-G are obtained successively from the continuity conditions at the boundaries Eq. (19) as

$$G = \sqrt{\mathcal{N}},$$

$$A = \frac{p_2}{p_A} G,$$

$$B = G,$$

$$C = -\frac{p_A}{2p_1}[A\cos(w_A p_A) - B\sin(w_A p_A)] - \frac{1}{2}[A\sin(w_A p_A) - B\cos(w_A p_A)],$$

$$D = \frac{1}{2} e^{2dp_1}\left[\left(A - \frac{p_A}{p_1}B\right)\sin(w_A p_A) - \left(\frac{p_A}{p_1}A + B\right)\cos(w_A p_A)\right],$$

$$E = \frac{p_1}{p_B}(D - Ce^{-2dp_1}),$$

$$F = Ce^{-2dp_1} + D,$$

$$H = -\frac{p_B}{p_2}[E\sin(w_B p_B) + F\cos(w_B p_B)]. \quad (22)$$

Finally, the composite-cavity mode frequencies $\Omega_j = ck_j$ are obtained from the positive solutions k_j of the transcendental equation

$$F\left(\frac{p_B}{p_2}\sin(p_B w_B) - \cos(p_B w_B)\right) = E\left(\frac{p_B}{p_2}\cos(p_B w_B) - \sin(p_B w_B)\right) \quad (23)$$

for the propagation constants.

Henceforth, we consider just two lateral composite-cavity modes $j=1,2$ and assume single-mode operation in the y and z directions ($l=1$, $m=1$). Consequently, the three-dimensional integral Eq. (15) simplifies to

$$\mathcal{K}_{aa'}^{A,B} = K_{jj'}^{A,B}\Gamma, \quad (24)$$

where

$$K_{jj'}^{A,B} = \frac{n_{A,B}^2 \int_{A,B} dx\, X_j(x) X_{j'}(x)}{2n_b^2(d_0 + w_0)}. \quad (25)$$

The confinement factor Γ describes the overlap between the composite-cavity modes and active media in the y and z directions:

$$\Gamma = \frac{\int_0^h dy\, Y_1^2(y)}{h} \frac{\int_0^L dz\, Z_1^2(z)}{(L/2)}. \quad (26)$$

Figure 2 shows $X_1(x)$ and $X_2(x)$ for a fixed stripe-width difference $\Delta w = w_B - w_A$ and three values of the half distance d. The black profile represents composite mode 1 with the higher frequency Ω_1, and the gray profile mode 2 with the lower frequency Ω_2. For $d=0$, the two composite-cavity modes become simply the two lowest-order modes of a single cavity of a combined width $w_A + w_B$ [Fig. 2(a)]. Since $w_A \neq w_B$, the amplitude of each composite-cavity mode in the different sections varies with the half distance d. In particular, for $w_A < w_B$ and increasing d, the amplitude of composite mode 1 in stripe A becomes smaller than in stripe B, and vice versa for mode 2 [Fig. 2(b)]. This difference increases with d as is demonstrated in Fig. 2(c).

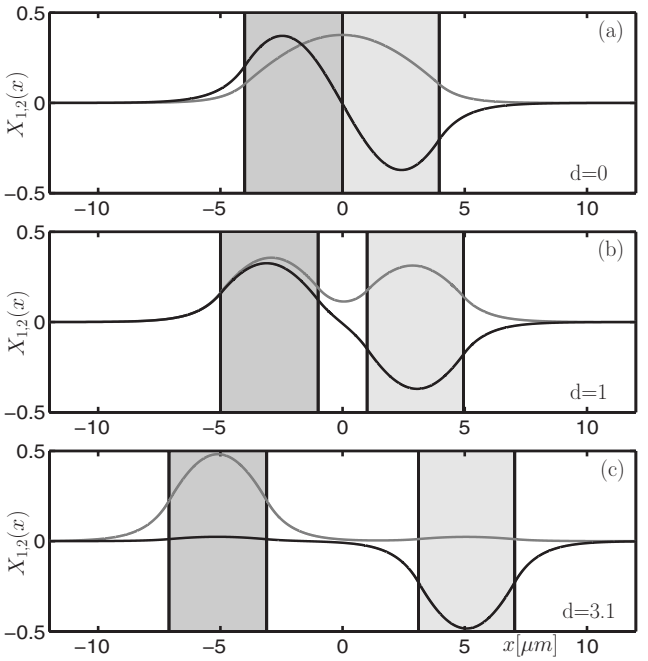

FIG. 2. x dependence of the two composite-cavity modes considered; the stripe-width difference is $\Delta w = -0.05$ μm and from (a) to (c) the half distance d is 0, 1, and 3 μm.

Under the assumption of single-mode operation in the y and z directions, $X_1(x)$ and $X_2(x)$ determine the dependence of $\Delta_{a,a'}$ of Eq. (7) and $K_{k,k'}^{A(B)}$ of Eq. (24) on the coupling conditions. Specifically, Fig. 3 shows the off-diagonal element $\Delta_{1,2}$ as a function of the half distance d and the stripe-

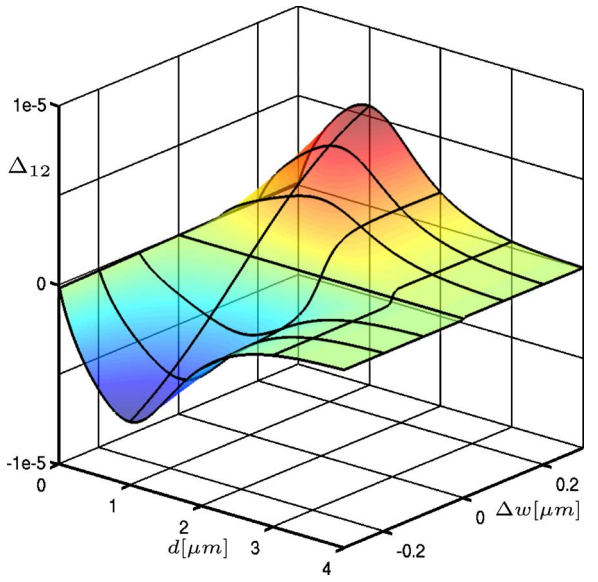

FIG. 3. (Color online) Off-diagonal matrix element $\Delta_{1,2}$ of Eq. (7) for the two composite-cavity modes as a function of the half distance d and the stripe-width difference Δw.

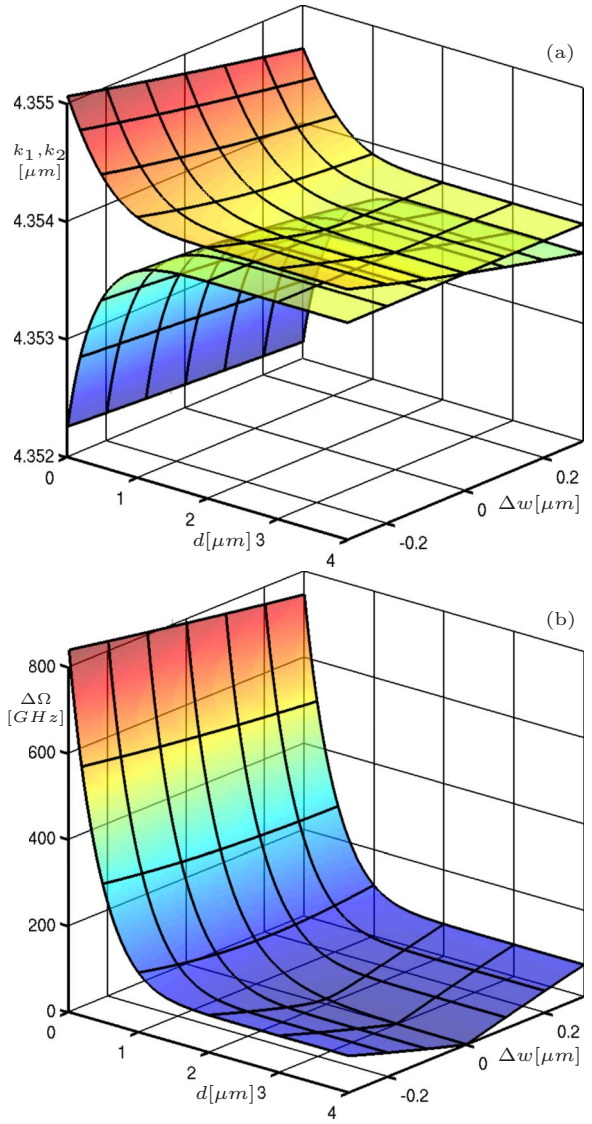

FIG. 4. (Color online) Magnitude of the wave vectors k_1 and k_2 (a) and the frequency detuning $\Delta\Omega = c(k_2 - k_1)$ (b) as a function of the half distance d and the stripe-width difference Δw.

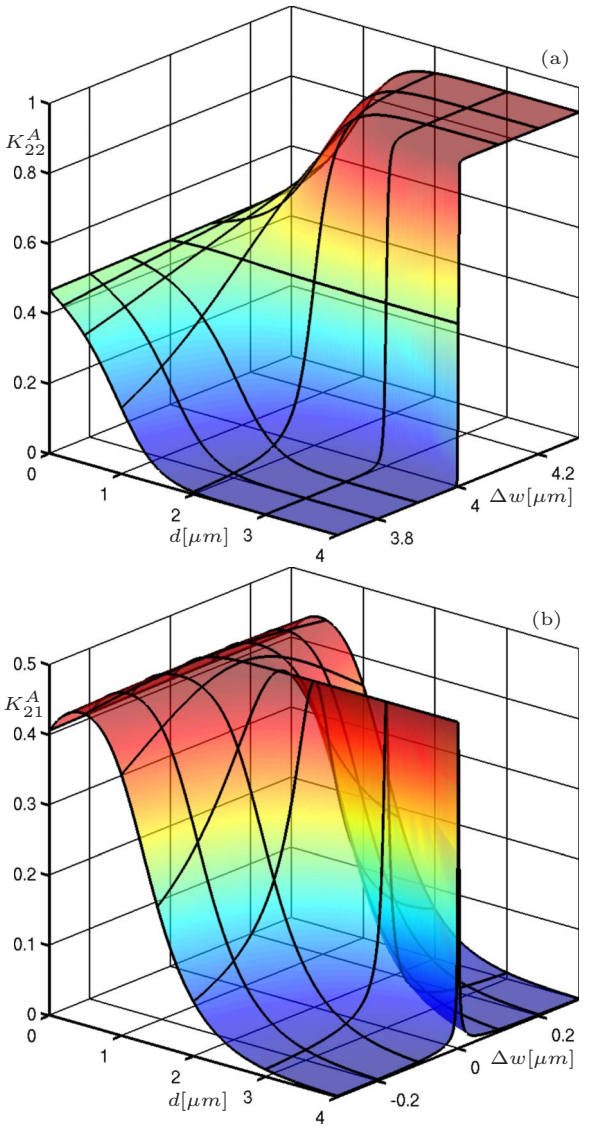

FIG. 5. (Color online) Modal gain coefficient K_{22}^A (a) and composite-mode coupling coefficient K_{21}^A (b) as a function of the half-distance d and the stripe-width difference Δw.

width difference Δw. Indeed, $\Delta_{a \neq a'} \lesssim 10^{-5}$ is negligible compared to $\Delta_{aa} \sim 1$, which justifies approximation (6) used in deriving the self-consistency equations (9) and (10) for our side-to-side coupled lasers. The dependence of the propagation constants k_1 and k_2 and the composite-mode frequency detuning $\Delta\Omega = c(k_2 - k_1)$ on d and Δw is plotted in Fig. 4. For large d (weak coupling), the frequency detuning $\Delta\Omega$ is a linear function of Δw and does not depend on d. However, for small d (strong coupling) the frequency detuning $\Delta\Omega$ becomes a strongly nonlinear function of d.

The self-consistency Eqs. (9) and (10) for the time evolution of the composite-cavity modes depend on the half distance d and the stripe-width difference Δw implicitly, via the modal overlap integrals Eq. (24). Specifically, $\mathcal{K}_{a=a'}^{A,B}$ are the modal gain and index-change coefficients and $\mathcal{K}_{a \neq a'}^{A,B}$ are the composite-mode coupling coefficients in stripes A and B. Figure 5(a) shows the dependence of K_{22}^A on d and Δw. For large d (weak coupling) the two composite-cavity modes approximate the modes of uncoupled lasers. For positive $\Delta w > 0$, $X_2(x)$ is almost completely located in laser A and therefore K_{22}^A is close to 1. [K_{22}^A is slightly less than one because $X_2(x)$ has nonzero amplitude in the passive regions.] For negative $\Delta w < 0$, $X_2(x)$ is almost completely located in laser B and therefore K_{22}^A is zero. At $\Delta w \approx 0$, there is a sharp change in the amplitude of each composite-cavity mode in the given laser. For small d (strong coupling) each composite-cavity mode has comparable amplitudes in both lasers. These amplitudes remain almost constant, $K_{22}^A \approx 0.5$, over a wide range of Δw. The plot for K_{22}^B is very similar after Δw is replaced with $-\Delta w$. Furthermore, a similar dependence is observed for K_{11}^A and K_{11}^B after Δw is replaced with $-\Delta w$. Figure 5(b) shows the dependence of K_{21}^A on d and Δw. For large d the coupling K_{21}^A is appreciable in just a small interval around $\Delta w \approx 0$. It drops to zero abruptly as $|\Delta w|$ increases. This is again due to the fact that for large d and $\Delta w \neq 0$ different composite modes are predominantly lo-

cated in different lasers. For small d, the amplitudes of both composite-cavity modes in each stripe are comparable and K_{21}^{A} remains appreciably nonzero over a wide range of Δw.

B. Dynamics of the composite-cavity model

Using Eqs. (9), (10), (12), (16), and (17), and rescaling the time and variables (see Appendix A), we arrive at the composite-cavity model,

$$\frac{d\tilde{E}_j}{d\tilde{t}} = -i(\tilde{\Omega}_j - \tilde{\nu}_j)\tilde{E}_j - \gamma\tilde{E}_j + \gamma\sum_{j'}\left(\sum_s K_{jj'}^s[(1+\beta\tilde{N}_s) - i\alpha\beta(1+\tilde{N}_s)]\right)\tilde{E}_{j'},$$

$$\frac{d\tilde{N}_s}{d\tilde{t}} = \tilde{\Lambda} - (\tilde{N}_s+1) - \sum_{j,j'} K_{jj'}^s(1+\beta\tilde{N}_s)\mathrm{Re}(\tilde{E}_j\tilde{E}_{j'}^*). \quad (27)$$

It governs the time evolution of the normalized electric field $\tilde{E}_j(\tilde{t})$ associated with each composite-cavity mode and the normalized carrier density $\tilde{N}_s(\tilde{t})$ in each laser. Here the index j refers to the composite mode 1 and 2, whereas s refers to the active region A and B, respectively; the asterisk denotes complex conjugation. In the remainder of this section we again drop the tildes for the rescaled quantities.

The simplest nontrivial solution to the composite-cavity model Eq. (27) is a continuous-wave (cw) solution, where both composite-cavity modes have constant amplitudes $|E_{1,2}^0|$ and are phase locked to a common frequency ω^0:

$$E_1(t) = |E_1^0|e^{-i\omega^0 t}, \quad E_2(t) = |E_2^0|e^{-i\omega^0 t - i\varphi},$$

$$N_A(t) = N_A^0, \quad N_B(t) = N_B^0. \quad (28)$$

Also, the carrier density $N_{A,B}^0$ in each laser is constant.

In the composite-cavity model, information about laser behavior needs to be extracted from the composite-cavity mode calculations. The total optical field inside lasers A and B arises from the combination of both composite-cavity modes. Here, we concentrate on the field in the center of each laser:

$$E_A(t) = X_1\left(d + \frac{w_A}{2}\right)E_1(t) + X_2\left(d + \frac{w_A}{2}\right)E_2(t),$$

$$E_B(t) = X_1\left(-d - \frac{w_B}{2}\right)E_1(t) + X_2\left(-d - \frac{w_B}{2}\right)E_2(t).$$

Hence, phase locking of the two lasers to a common frequency can be achieved in two different ways: via phase locking of the composite-cavity modes, or when just one composite-cavity mode has a non-negligible amplitude [Eq. (28)].

To get a first impression of the possible dynamics of the composite-cavity model, including different mechanisms leading to phase locking or dynamical instabilities, we plot in Fig. 6 bifurcation diagrams as a function of the half distance d for $\Delta w = 0.02$ and three different values of α. The bifurcation diagrams have been calculated by numerical time integration of Eqs. (27). Note that this means that the spatial mode problem outlined in Sec. III A has to be solved for each combination of the coupling parameters d and Δw to determine the modal frequencies Ω_j as well as the gain and coupling coefficients $K_{jj'}^s$. Figure 6 shows the local extrema of the modal intensities $I_1(t) = |E_1(t)|^2$ and $I_2(t) = |E_2(t)|^2$, as well as the resulting total intensity $I_A(t) = |E_A(t)|^2$ in laser A. For $\alpha = 0$ [Fig. 6(a)] the dynamics is dominated by cw solutions and periodic intensity oscillations; there is only a small interval around $d \approx 2.2$ with complicated dynamics. Specifically, for very small d composite mode 1 is on (has nonzero intensity) but composite mode 2 is off (has negligible intensity): $(I_1; I_2) \approx (\Lambda; 0)$. At around $d \approx 0.1$, composite mode 1 is off and composite mode 2 is on: $(I_1; I_2) \approx (0; \Lambda)$. In both cases the total intensity in laser A is constant. However, the switch over from composite mode 1 to 2 appears as a discontinuity in the total intensity I_A at $d \approx 0.1$. At $d \approx 1.6$ the cw solution bifurcates into intensity oscillations. After a small window with complicated dynamics around $d = 2.2$, the system settles back to periodic intensity oscillations with comparable amplitudes of both composite modes. Already for $\alpha = 0.4$ [Fig. 6(b)] the behavior is much more complicated. For $d = 0$, the system is settled to the cw solution $(I_1; I_2) \approx (\Lambda; 0)$, then switches to the reverse situation $(I_1; I_2) \approx (0; \Lambda)$, and returns to $(I_1; I_2) \approx (0; \Lambda)$ around $d = 0.5$. Periodic intensity oscillations appear at around $d = 1.5$ from the cw solution $(I_1; I_2) \approx (\Lambda; 0)$. As d is increased, these oscillations undergo further bifurcations leading to complicated dynamics. For $\alpha = 2.0$ [Fig. 6(c)] the solution with $(I_1; I_2) \approx (0; \Lambda)$ for small d has disappeared. Also, the parameter interval with complicated dynamics has increased. At around $d = 2.8$ there is a window with stable cw solution where both composite modes have comparable intensities. In this window, the two composite modes are phase-locked, so the total intensity in laser A is constant. Again periodic oscillations can be found for $d > 3$.

Taken together, Fig. 6 identified parameter regions where the coupled-laser device shows constant intensity operation or complicated dynamics. In particular, constant intensity operation is of a different dynamical flavor. For weak coupling there is phase locking of composite-cavity modes with comparable intensities, but for strong coupling there is strong mode competition, so that one mode is dominant and the other mode has negligible intensity. Complicated dynamics arises in the intermediate parameter region.

1. Continuous wave operation

In order to gain better insight into the dynamics of the side-to-side coupled laser system, in particular, mechanisms leading to cw operation of the composite-cavity modes, we now present a comprehensive bifurcation study using numerical continuation [60,61]. This approach allows us to identify regions of stable cw solutions given by Eq. (28) in the two-dimensional parameter plane of half distance d and stripe-width difference Δw. These regions are bounded by bifurcation curves, namely, curves of saddle-node bifurcations, where a pair of cw solutions is created, and Hopf bifurcations, where a cw solution bifurcates into a periodic

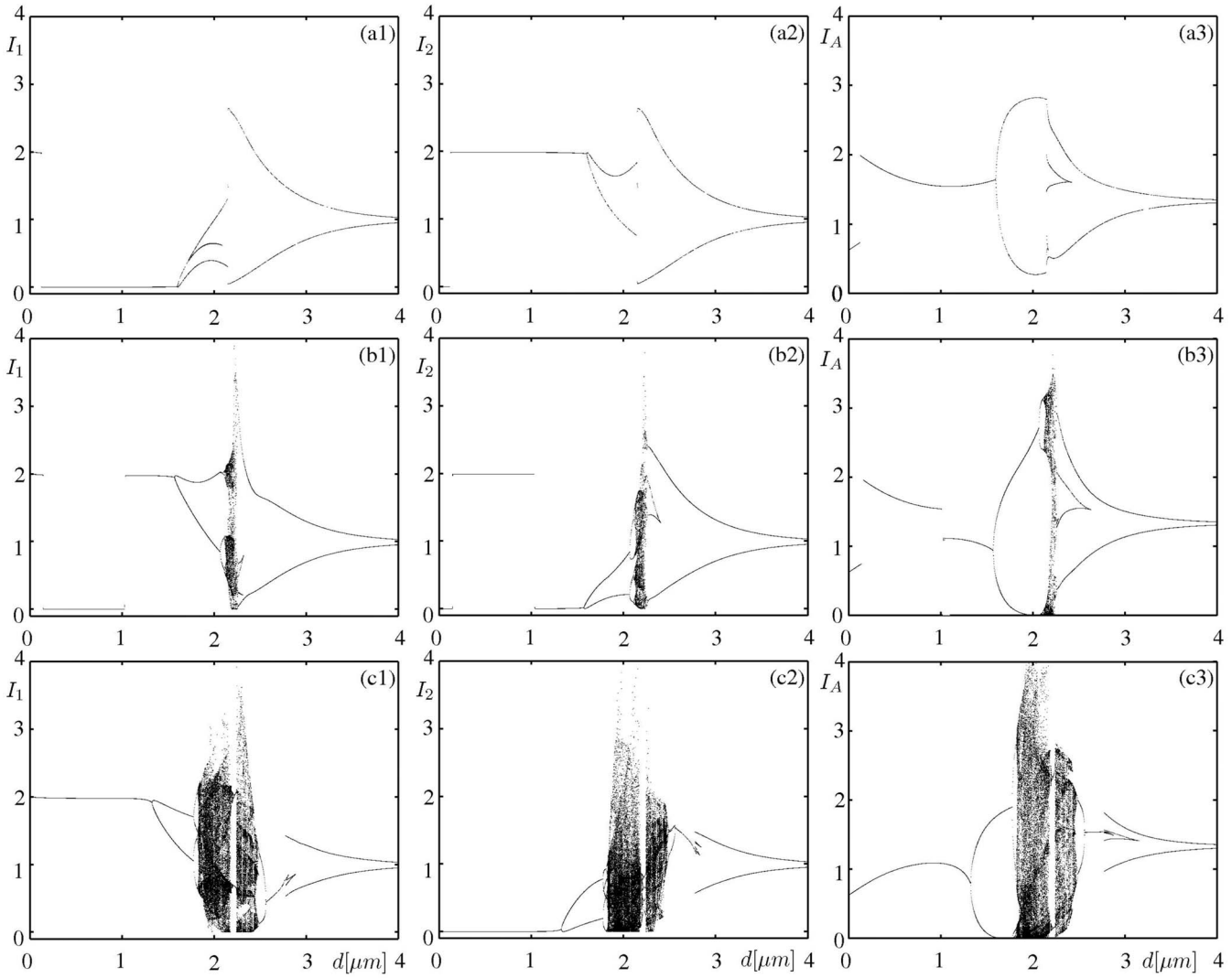

FIG. 6. One-parameter bifurcation diagrams of the composite-cavity model, shown as extrema of the intensity in composite mode 1, mode 2, and laser stripe A; throughout $\Delta w=0.02$ and from rows (a) to (c) α has the values 0, 0.4, and 2.0.

intensity oscillation. Figure 7 shows regions of stable cw solutions of the composite-cavity model Eq. (27) and their bifurcations in the $(d,\Delta w)$ plane for different values of the linewidth enhancement factor α. The hatching indicates regions with stable cw solution, where the different hatching distinguishes between different stable cw solutions observed in Fig. 6. Thick bifurcation curves indicate that the bifurcating solution is stable and thin bifurcation curves indicate that it is unstable.

Figure 7(a) shows the situation for $\alpha=0$. For large d stable cw solutions arise from saddle-node bifurcations (S) around Δw zero. Note that what appears to be a single saddle-node curve are actually two saddle-node curves very close to each other, each giving rise to one stable cw solution. Hence the cross hatching, which indicates bistability of two stable cw solutions. For decreasing d, one of the cw solutions undergoes a subcritical Hopf bifurcation. For even smaller d, the other cw solution also loses stability in a subcritical Hopf bifurcation ($d\approx 0.01$ μm). A second Hopf bifurcation close by leads to another short interval with stable cw solution for even smaller d (right-inclined hatch). Note that in Fig. 6(a) this transition at $d\approx 0.01$ was observed as a discontinuous change in the intensity of laser A. Furthermore, we find points where the boundary of the locking region changes from a saddle-node curve to a Hopf bifurcation. These special codimension-2 bifurcation points are called saddle-node Hopf (SH) points. In total there are four saddle-node Hopf points, two for each cw solution. Degenerate Hopf (DH) points indicate points where there is a change on a Hopf bifurcation curve from super- to subcritical Hopf bifurcations.

For $\alpha=0.32$ in Fig. 7(b) the two previously overlapping saddle-node curves have clearly separated. For small d the cw solution is still dominated by one composite mode. Depending on the value of d either composite mode 1 or 2 is dominant. Furthermore, in Fig. 7(b), the upper and the lower supercritical Hopf branches approach each other around $(d,\Delta w)=(1.2;0)$. This indicates that in the three-dimensional $(d,\Delta w,\alpha)$ parameter space, Hopf bifurcations form two-dimensional surfaces with saddle points. In the $(d;\Delta w)$ plane, a transition through a saddle point in the surface of

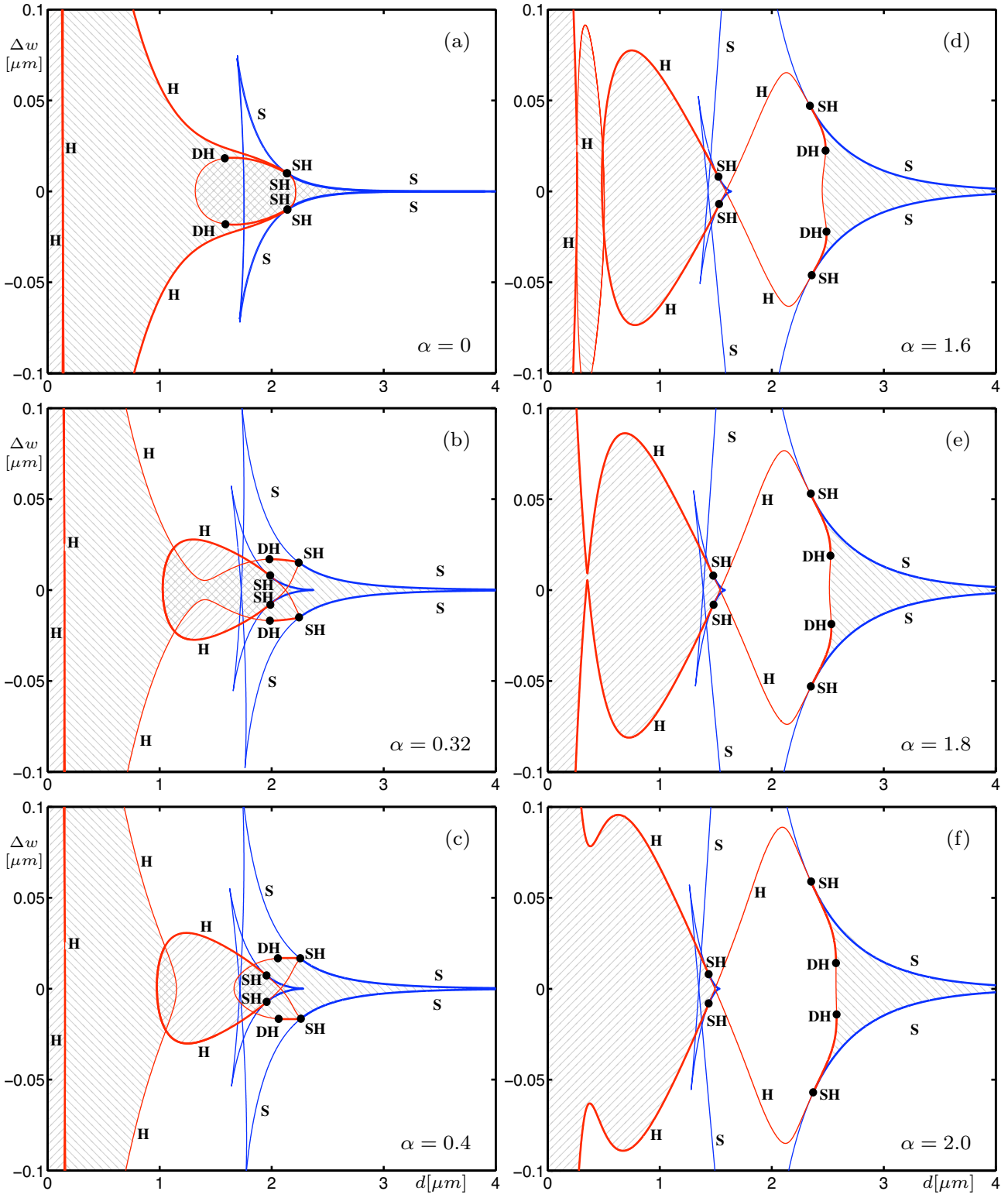

FIG. 7. (Color online) Two-parameter bifurcation diagram in the $(d,\Delta w)$ plane of the composite-cavity model for different values of α as indicated in the individual panels. Shown are curves of saddle-node (S) and Hopf (H) bifurcations; codimension-2 saddle-node Hopf (SH) and degenerate Hopf (DH) bifurcations occur at isolated points; hatched regions indicate stable cw solution.

Hopf bifurcations rearranges the Hopf branches, as can be seen in Fig. 7(c) for α=0.4.

When increasing α from 0.4 to 1.6, as shown in Fig. 7(d), the Hopf branches change near the saddle-node Hopf points; namely, at a particular value of α the Hopf curve has a cusp singularity at SH—a transition that is commonly found in laser systems [37,62]. (Also, see Ref. [63] for details of the possible different unfoldings of saddle-node Hopf points.) As

a consequence the stability regions of the cw solutions become further untangled. Notably, in Fig. 7(d) there is no longer a bistability region and a gap without any stable cw solution has formed. Specifically, as we go from large toward small d around $\Delta w \approx 0$ we find stable cw solutions, characterized by phase-locked composite modes. They lose stability in a Hopf bifurcation, but for smaller d we again find stable cw solutions. Note that there are three different regions bounded by Hopf bifurcations, where only one of the composite-cavity modes has non-negligible amplitude.

As α is increased further, the region with stable cw solution for small d disappears; see Fig. 7(e). Furthermore, two stability regions merge in a saddle-point singularity of a two-dimensional Hopf bifurcation surface in the $(d, \Delta w, \alpha)$ parameter space. Eventually, this leads to two regions with stable cw solutions separated by a gap, as is shown in Fig. 7(f). The stable cw solution for small d is associated with operation in only one composite mode, namely, mode 1, and its region of stability extends to large Δw. The stable cw solution for large d, on the other hand, is associated with phase-locked operation of both composite modes. It is bounded by a saddle-node curve toward increasing $|\Delta w|$.

2. Beyond continuous-wave operation

Figures 6 and 7 already indicate that one must expect more complex and possibly chaotic dynamics of the side-to-side coupled lasers. In order to study the dynamics beyond stable cw solutions we focus on periodic solutions where $|E_{1,2}|$, $N_{A,B}$ and $|\Phi_1 - \Phi_2|$ oscillate, and consider their bifurcations. These bifurcations include saddle-node of limit-cycle (SL) bifurcations, where a pair of periodic solutions is created, period-doubling (PD) bifurcations, where a periodic solution with twice the period bifurcates from the initial periodic solution, and torus (T) bifurcations, where a second frequency is introduced into the system. Finally, we also find homoclinic (hom) bifurcations, which occur as the result of a rearrangement of stable and unstable manifolds of a saddle cw solution; physically, the period of the associated intensity oscillation goes to infinity. See, for example, Refs. [63,64] for more background information on these bifurcations. The different bifurcations of periodic solutions are organized into an overall bifurcation diagram. Importantly, points of codimension-2 bifurcation organize the overall structure.

Figure 8 shows the bifurcation diagram of the composite-cavity model Eq. (27) in the $(d, \Delta w)$ plane with bifurcations of emerging periodic solutions for three different values of α. Here we concentrate on the region of intermediate values of d near to the codimension-2 bifurcation points and do not distinguish between super- and subcritical bifurcations of periodic solutions. Since the bifurcation diagrams are almost symmetrical with respect to the detuning, we will discuss only the upper half where $\Delta w \geqslant 0$.

Figure 8(a) shows the situation for $\alpha = 0$. As was explained earlier, there are two saddle-node curves almost on top of each other. Both change criticality in two saddle-node Hopf points. From each point SH a curve T of torus bifurcations emerges. The other end point of each torus curve is a (1:2) resonance point, where the curve T ends on a curve P of period-doubling bifurcations. Furthermore, there is a curve

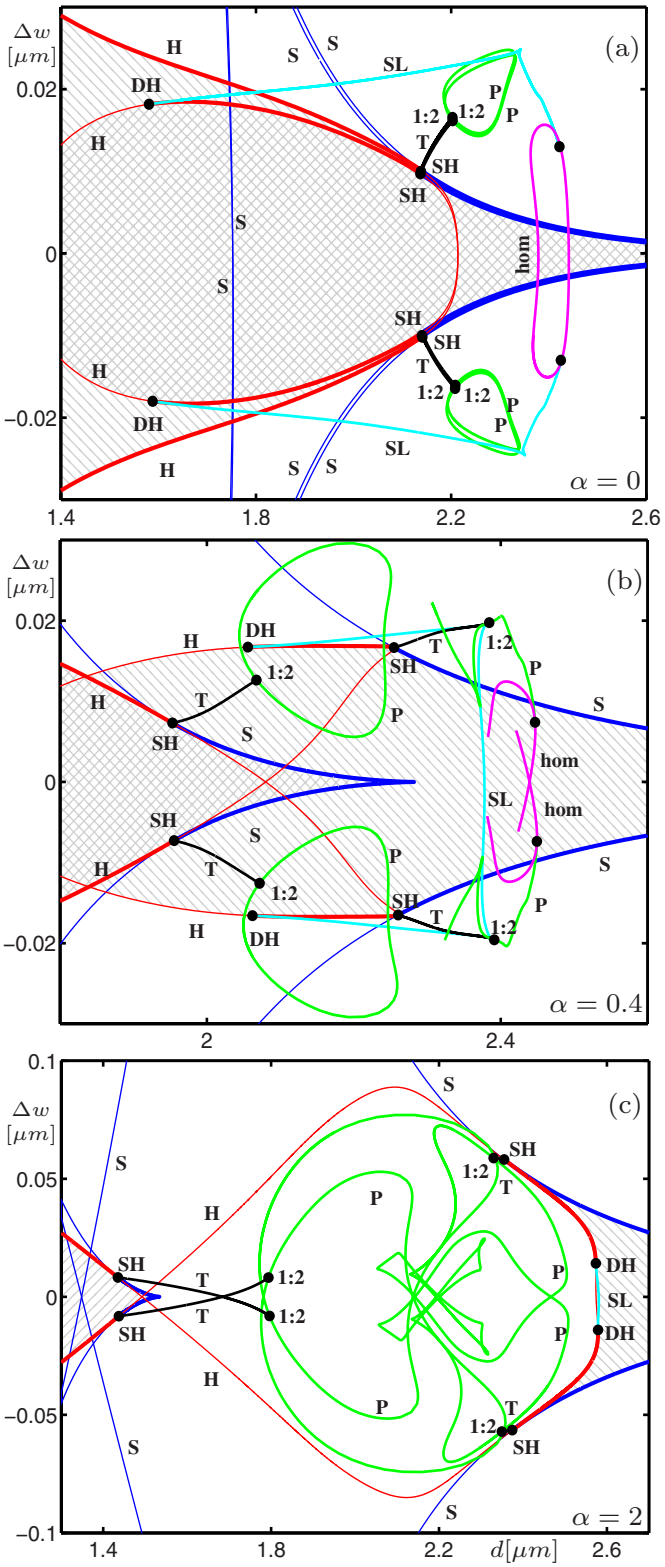

FIG. 8. (Color online) Two-parameter bifurcation diagram in the $(d, \Delta w)$ plane of the composite-cavity model, showing also bifurcations of periodic solutions for three different values of α as shown in the panels. Additional curves are those of period doubling (P), torus (T), saddle-node (SL) of limit cycles, and homoclinic (hom) bifurcations; additional codimension-2 bifurcations are points of 1:2 resonance bifurcation and degenerate homoclinic points (B) points. Hatched regions indicate stable cw solution.

SL of saddle-node of limit-cycle bifurcations. It ends for small d in a degenerate Hopf point DH, where the Hopf bifurcation curve changes its criticality. The other end point of the curve SL is a point on a curve hom of homoclinic bifurcations, where the periodic solution bifurcating from the curve hom changes its stability. Notice that, overall, the bifurcations associated with periodic solutions are located in a relatively small area of the $(d,\Delta w)$ plane, well above and below the horizontal axis where $\Delta w=0$.

Figure 8(b) shows the bifurcation diagram for $\alpha=0.4$. As was already observed previously, the two stable cw solutions and their bifurcations have untangled. The two previously overlapping saddle-node Hopf points SH are clearly separated. The overall bifurcation structure is now quite complicated. In particular, bifurcations associated with periodic solutions can now be found in a much larger part of the $(d,\Delta w)$ plane and overlapping with the stability regions of cw solutions. From each SH point a torus curve T emerges and terminates at a (1:2) resonance point. One period-doubling curve still forms a closed loop, but a second period-doubling curve has a much more complicated structure and it ends at a point on the curve of homoclinic bifurcations. Furthermore, there is a curve SL of saddle-node of limit cycle bifurcations, which now connects the two degenerate Hopf points on the upper and the lower detuning half plane.

Finally, for $\alpha=2$ as in Fig. 8(c), the main structural elements, i.e., the codimension-2 points, of the bifurcation diagram are preserved. The main differences are due to the cusp transition of the Hopf curve at the SH point at large d that gives rise to the intermediate region without stable cw solution. As a consequence, the torus curve emerging from this SH point is now located on the other side of the curve S. Note that the two end points of this torus branch, i.e., the SH point and the (1:2) resonance point, are now very close together. Furthermore, there is a short curve of saddle-node bifurcation of limit cycle (SL) for large d that connects the two DH points. The main feature for $\alpha=2$ is that the bifurcations associated with periodic solutions have now moved into the region without stable cw solution. They cover a large region around the horizontal axis of the $(d,\Delta w)$ plane, so that they can now be found even for $\Delta w=0$. This agrees with the observation in Fig. 6(c) that the locking intervals characterized by stable cw solutions are separated by a window of complicated, possibly chaotic dynamics.

IV. WEAK-COUPLING THEORY

A composite-cavity model describes the spatiotemporal dynamics of a given laser structure for arbitrary coupling conditions. The previous section discussed the case of a simple two-laser system. In case of (more complicated) two-dimensional laser arrays, constructing orthogonal composite-cavity modes as required by semiclassical laser theory may be a rather difficult or even impractical task. In such a situation one may desire a simpler model which, nevertheless, possesses the necessary components to reproduce the general aspects of nonlinear behavior. Therefore, we now ask whether one can find a simpler rate equation model that still reproduces relevant aspects of the dynamics that are found in the more accurate composite-cavity model.

Assuming weak-coupling conditions can immensely simplify the solution of the wave equation (1), and this leads to simple rate equation models. Such models, which describe the interaction between individual lasers rather than modes of the entire coupled-laser structure, have been used extensively in previous studies of coupled-laser systems. Most commonly used is the individual-laser model. As we will show in the next section, the individual-laser model for two side-to-side coupled lasers has a bifurcation diagram that is significantly different from the one obtained for the composite-cavity model. The uncovered disagreement motivates the derivation of the coupled-laser model in Sec. IV C, which captures the relevant dynamics of the composite-cavity model, provided the coupling is not too strong.

A. Individual-laser theory

In individual-laser theory the wave equation (1) is solved by assuming that different lasers of the array are completely uncoupled. Specifically, the wave equation for each individual single-mode laser can be written as

$$n_A^2 k_A^2 \mathcal{E}_A + \mu_0 \sigma \dot{\mathcal{E}}_A + \frac{n_A^2}{c} \ddot{\mathcal{E}}_A = -\mu_0 \ddot{\mathcal{P}}_A,$$

$$n_B^2 k_B^2 \mathcal{E}_B + \mu_0 \sigma \dot{\mathcal{E}}_B + \frac{n_B^2}{c} \ddot{\mathcal{E}}_B = -\mu_0 \ddot{\mathcal{P}}_B, \tag{29}$$

where $\mathcal{E}_{A,B}$ is the total intracavity field of lasers A and B. In the slowly varying amplitude and phase approximation, Eqs. (29) become

$$\dot{E}_A + \left(\frac{\sigma}{2\epsilon_0 n_A^2} + i(\Omega_B - \nu) \right) E_A = \frac{i\nu}{2\epsilon_0 n_A^2} P_A,$$

$$\dot{E}_B + \left(\frac{\sigma}{2\epsilon_0 n_B^2} + i(\Omega_A - \nu) \right) E_B = \frac{i\nu}{2\epsilon_0 n_B^2} P_B, \tag{30}$$

where we introduced the cavity resonance frequencies $\Omega_{A,B} = ck_{A,B}$. At this stage of the derivation, coupling between the lasers is introduced by adding a coupling term to the right-hand side of the electric field equation (30) of each laser. Using the simplified model (12) for the polarization of a semiconductor medium in Eqs. (30) and rescaling time and variables (Appendix A), one arrives at the individual-laser model,

$$\frac{d\tilde{E}_{A,B}}{dt} = -i(\tilde{\Omega}_{A,B} - \tilde{\nu})\tilde{E}_{A,B}, + (1 - i\alpha)\beta\gamma \tilde{N}_{A,B}\tilde{E}_{A,B} + \kappa \tilde{E}_{B,A},$$

$$\frac{d\tilde{N}_{A,B}}{dt} = \tilde{\Lambda} - (\tilde{N}_{A,B} + 1) - (1 + \beta \tilde{N}_{A,B})|\tilde{E}_{A,B}|^2. \tag{31}$$

It governs the time evolution of the normalized complex-valued optical fields $\tilde{E}_{A,B}$ and normalized real-valued carrier densities $\tilde{N}_{A,B}$ of lasers A and B. In the remainder of this section we again drop the tildes for the rescaled quantities for convenience. Both lasers are assumed to be the same, mean-

ing that they have the same values of the linewidth enhancement factor α, the dimensionless gain parameter β, the ratio of the field and carrier decay rates γ, and the pump parameter Λ. However, they may have a frequency difference or detuning

$$\Delta\Omega = \Omega_B - \Omega_A. \tag{32}$$

In principle, the coupling parameter in Eqs. (31) could be introduced as complex valued. In this case the question arises as to what the right value of the coupling phase (the argument of the complex-valued coupling parameter) might be in a given laser setup; this issue is addressed in Sec. IV C. However, the majority of investigators [13,31,38–45,65] choose the coupling phase to be zero, and this is also what we did in Eqs. (31). Furthermore, for the side-to-side coupled lasers, the coupling arises due to the overlap of the laser electric field profiles (evanescent waves) in the lateral x direction. Hence, the coupling parameter κ is assumed to decrease exponentially [13] with the distance between the lasers, as

$$\kappa = \frac{C}{\gamma_N} \exp(-2dp_G). \tag{33}$$

Here C is the coupling rate in units of inverse seconds and p_G is the inverse coupling length. Because the introduction of coupling terms in Eq. (31) and the assumption of the exponential scaling in Eq. (33) are purely phenomenological, this modeling approach does not give any information about the values of C and p_G. For reasons of comparability that will become clear in Sec. IV C, we choose constant values $C/\gamma_N = 420$ and $p_G = 0.98\ \mu\text{m}^{-1}$.

Due to their simplicity, Eqs. (31) have been used extensively in the literature to model the dynamical behavior of various coupled-laser systems [13,31,38–45,65]. The common assumption in studies using this model is that it is valid only for low values of the coupling parameter κ, i.e., the coupling is seen as a small perturbation of the solitary laser.

B. Dynamics of the individual-laser model

The cw solutions of Eqs. (31) have the form

$$E_A(t) = |E^0| e^{-i\omega^0 t}, \quad N_A(t) = N^0,$$

$$E_B(t) = |E^0| e^{-i\omega^0 t - i\varphi}, \quad N_B(t) = N^0. \tag{34}$$

Notably, the time-independent amplitudes $|E^0|$ and carrier densities N^0 in both lasers are identical, even for nonzero detuning, $\Omega_A \neq \Omega_B$. Inserting ansatz (34) into Eqs. (31) gives two cw solutions,

$$|E^0|_\pm = \sqrt{\frac{\Lambda - 1 \pm (\kappa/\beta\gamma)\sqrt{1 - (\Delta\Omega/2\kappa)^2}}{1 \mp (\kappa/\gamma)\sqrt{1 - (\Delta\Omega/2\kappa)^2}}}, \tag{35}$$

$$N^0_\pm = \mp \frac{\kappa}{\gamma\beta}\sqrt{1 - \left(\frac{\Delta\Omega}{2\kappa}\right)^2}, \tag{36}$$

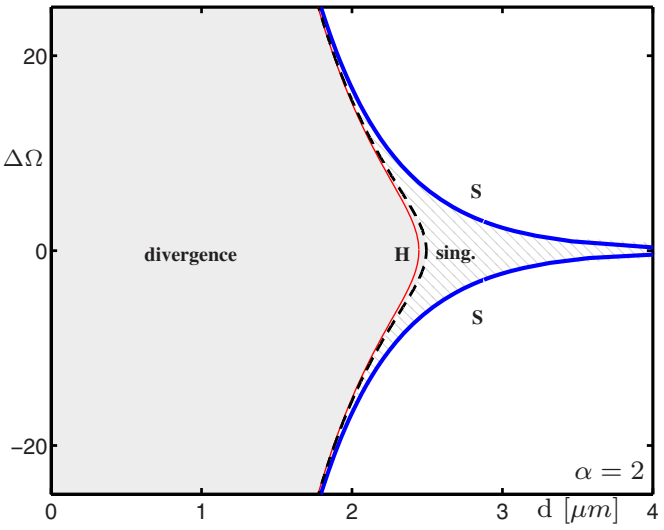

FIG. 9. (Color online) Two-parameter bifurcation diagram in the $(d, \Delta\Omega)$ plane of Eqs. (31) for $\alpha = 2.0$ with saddle-node bifurcation (S), Hopf bifurcation (H), and the cw singularity curve. The hatched region indicates the stable cw solution and the gray shaded region divergence of the model.

$$\omega^0_\pm = \frac{\Delta\Omega}{2} - \alpha\beta N^0_\pm, \tag{37}$$

$$\varphi = \arcsin\left(\frac{-\Delta\Omega}{2\kappa}\right) + m\pi, \tag{38}$$

of which $(|E^0|_+, N^0_+, \omega^0_+, \varphi)$ is stable and $(|E^0|_-, N^0_-, \omega^0_-, \varphi)$ is unstable. Interestingly, Eq. (35) for the normalized field intensity $|E^0|^2_+$ of the only stable cw solution has a singularity when

$$1 = \frac{\kappa}{\gamma}\sqrt{1 - \left(\frac{\Delta\Omega}{2\kappa}\right)^2}. \tag{39}$$

Figure 9 shows the bifurcation diagram of the individual-laser model Eqs. (31) in the $(d, \Delta\Omega)$ plane for $\alpha = 2.0$. The two cw solutions are created in the saddle-node bifurcation (S). In the hatched region the stable cw solution exists with finite field amplitude. For parameters above the upper branch of S and below the lower branch of S the lasers are unlocked, meaning that each laser operates at a different frequency and the intensity of the light emitted oscillates periodically. Starting on S and decreasing the half distance d for fixed $\Delta\Omega$ (hence, increasing the coupling strength), the intensity of the stable cw solution $|E^0|^2_+$ slowly increases and then diverges off to infinity at the singularity given by Eq. (39), which occurs along the dashed curve in Fig. 9. To the left of the dashed singularity curve the only attractor is a cw solution with infinite intensity. The Hopf bifurcation curve (H) in Fig. 9 indicates a Hopf bifurcation of the unstable cw solution. Figure 9 shows the situation for $\alpha = 2.0$ only because the diagram does not depend on α (except for the position of the Hopf bifurcation of the unstable cw solution). We remark that for the case of a solid-state laser Eqs. (31) give rise to additional bifurcations and a small region of complicated

$\alpha = 0.4$

dynamics [38]. However, for parameter values describing a semiconductor laser as considered here, we found no bifurcations of periodic orbits nor chaos.

Comparison between Secs. III B and IV B shows that bifurcations of the composite-cavity model (27) and the individual-laser model (31) are drastically different. In fact, none of the relevant dynamics found in the composite-cavity model (27) including bistability, complicated intensity oscillations, and strong dependence of the locking region on α, appears in the individual-laser model (31).

C. Coupled-laser theory

The previous section provides the motivation for developing a simple model that can reproduce the dynamics of the more accurate composite-cavity model, at least for weak coupling. More specifically, we derive simple rate equations for two single-mode lasers coupled side to side, where we use the semiclassical theory of coupled lasers developed by Spencer and Lamb in Refs. [1,2]. A difference with these works is that we apply the general concept of a laser with transmitting interface to our case of lasers that are coupled side to side via evanescent fields. Furthermore, the lasers are coupled via a passive section of different refractive index rather than a (infinite) refractive index "bump." To facilitate the calculations we consider two identical lasers, whose fields are not leaking to the outside world, i.e., $\mathcal{E}(x,t)=0$ for $|x| \geqslant (d+w_{A,B})$, and that are coupled due to some field leaking at $x=\pm d$. The situation is shown in Fig. 10. Under weak-coupling conditions, where the electric fields at $x=\pm d$ are small, one can expand the intracavity fields of lasers A and B in terms of the normal modes of a closed cavity, which vanish at $x=\pm d$ and $x=\pm(d+w_{A,B})$. Although the electric field in each laser has a space-dependent component that vanishes at $x=\pm d$, we still account for the fact that there is a small electric field at $x=\pm d$ in Maxwell's equations. Following Ref. [1], the resulting wave equation for the optical fields inside lasers A and B can be approximated by

$$n_A^2 k_A^2 \mathcal{E}_A + \mu_0 \sigma \dot{\mathcal{E}}_A + \frac{n_A^2}{c}\ddot{\mathcal{E}}_A = -\mu_0 \ddot{\mathcal{P}}_A + \frac{2p_A}{w_A}\mathcal{E}(-d,t),$$

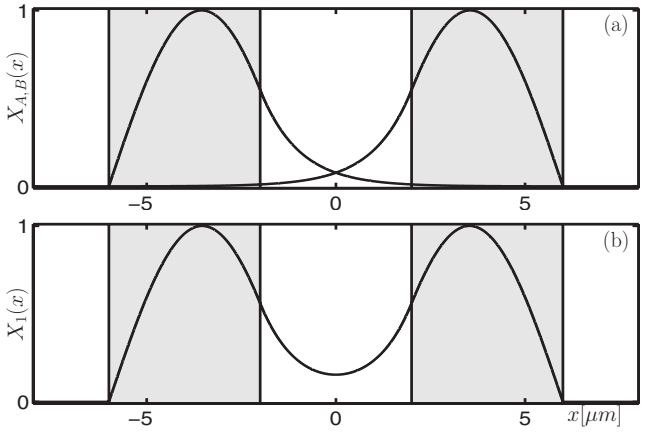

FIG. 10. x dependence of the electric fields of each individual laser (a) and the total electric field inside the coupled-laser device (b).

$$n_B^2 k_B^2 \mathcal{E}_B + \mu_0 \sigma \dot{\mathcal{E}}_B + \frac{n_B^2}{c}\ddot{\mathcal{E}}_B = -\mu_0 \ddot{\mathcal{P}}_B + \frac{2p_B}{w_B}\mathcal{E}(d,t). \quad (40)$$

In contrast to the individual-laser model (31), the coupling between lasers is taken into account already when the wave equation (1) is solved. It is represented by the additional source terms in the right-hand side of Eqs. (40), proportional to $\mathcal{E}(-d,t)$ and $\mathcal{E}(d,t)$, which reflect the fact that the total field at $x=\pm d$ is not quite zero [2]. In the side-to-side coupling configuration each coupling term depends on the lateral component $p_{A,B}$ of the wave vector.

Figure 10(a) shows transversal field profiles of lasers A and B as if the lasers were uncoupled. For coupled lasers we need to know the total electric field inside laser A, inside laser B, and inside the passive section between the lasers in order to evaluate $\mathcal{E}(-d,t)$ and $\mathcal{E}(d,t)$ in Eqs. (40). The total space- and time-dependent electric field inside the coupled-laser system can be written as

$$\mathcal{E}(x,t) = \begin{cases} \mathcal{E}_A(t)\sin[p_A(x+d+w_A)] & \text{if } -d-w_A \leqslant x \leqslant -d, \\ \mathcal{E}_{G1}(t)e^{-p_G(x+d)} + \mathcal{E}_{G2}(t)e^{p_G(x-d)} & \text{if } -d \leqslant x \leqslant d, \\ \mathcal{E}_B(t)\sin[p_B(x-d-w_B)] & \text{if } d \leqslant x \leqslant d+w_B. \end{cases} \quad (41)$$

Figure 10(b) depicts its spatial dependence. Specifically, the total field in the passive gap between the two lasers is a superposition of two evanescent fields leaking out of lasers A and B.

From the boundary conditions for the total electric field $\mathcal{E}(x,t)$,

$$\mathcal{E}(-d-w_B,t) = 0,$$

$$\mathcal{E}(d+w_A,t) = 0,$$

$$\mathcal{E}(-d^-,t) - \mathcal{E}(-d^+,t) = 0,$$

$$\frac{\partial}{\partial x}\mathcal{E}(-d^-,t) - \frac{\partial}{\partial x}\mathcal{E}(-d^+,t) = 0,$$

$$\mathcal{E}(d^-,t) - \mathcal{E}(d^+,t) = 0,$$

$$\frac{\partial}{\partial x}\mathcal{E}(d^-,t) - \frac{\partial}{\partial x}\mathcal{E}(d^+,t) = 0, \tag{42}$$

we obtain the fields at transmitting interfaces as

$$\mathcal{E}(-d,t) = \frac{\mathcal{E}_A(t)}{2}\left(\sin(p_A w_A) - \frac{p_A}{p_G}\cos(p_A w_A)\right),$$

$$-\frac{\mathcal{E}_B(t)}{2}e^{-2p_G d}\left(\sin(p_B w_B) - \frac{p_B}{p_G}\cos(p_B w_B)\right), \tag{43}$$

$$\mathcal{E}(d,t) = -\frac{\mathcal{E}_B(t)}{2}\left(\sin(p_B w_B) - \frac{p_B}{p_G}\cos(p_B w_B)\right)$$

$$+\frac{\mathcal{E}_A(t)}{2}e^{-2p_G d}\left(\sin(p_A w_A) - \frac{p_A}{p_G}\cos(p_A w_A)\right), \tag{44}$$

and derive the transcendental equation

$$-\left(\sin(p_B w_B) + \frac{p_B}{p_G}\cos(p_B w_B)\right)\left(\sin(p_A w_A) - \frac{p_A}{p_G}\cos(p_A w_A)\right)$$
$$= \left(\sin(p_A w_A) + \frac{p_A}{p_G}\cos(p_A w_A)\right)\left(\sin(p_B w_B) - \frac{p_B}{p_G}\right.$$
$$\left.\times\cos(p_B w_B)\right)\exp[-4dp_G], \tag{45}$$

which determines the values of the propagation constants $p_{A,B}$ and p_G.

Using expressions (43) and (44) for $\mathcal{E}(-d,t)$ and $\mathcal{E}(d,t)$ we rewrite Eqs. (40) in the slowly varying amplitude and phase approximation as

$$\dot{E}_A + \left(\frac{\sigma}{2\epsilon_0\epsilon_A} + i(\Omega'_B - \nu + C)\right)E_A$$
$$= \frac{i\nu}{2\epsilon_0 n_A^2}P_A + iC\exp[-2dp_G]E_B,$$

$$\dot{E}_B + \left(\frac{\sigma}{2\epsilon_0\epsilon_B} + i(\Omega'_A - \nu + C)\right)E_B$$
$$= \frac{i\nu}{2\epsilon_0 n_B^2}P_B + iC\exp[-2dp_G]E_A, \tag{46}$$

where $\Omega'_{A,B} = ck_{A,B}$. Furthermore, in the derivation of the coupling rate

$$C = \frac{cp}{2wn_b^2 k}\left[\sin(pw) - \frac{p}{p_G}\cos(pw)\right], \tag{47}$$

we assumed $w = w_A \approx w_B$, $n_b = n_A \approx n_B$, and $p = p_A \approx p_B$. As can be seen from Eqs. (46) the partially transmitting interface introduces a small shift C in the lasing frequency, and coupling between lasers gives rise to an additional source term $iC\exp(-2dp_G)$ on the right-hand side.

In order to calculate the inverse coupling length p_G and the coupling rate C for the laser geometry considered in Fig. 10, we need relations between the propagation constants p, p_G, and the total wave number k. With the ansatz Eq. (41) we obtain these relations from Eq. (18) as

$$-p^2 + n_b^2 k^2 - k_z^2 = 0,$$

$$p_G^2 - k_z^2 + n_G^2 k^2 = 0, \tag{48}$$

with $k_z = 5\pi \times 10\ \mathrm{m}^{-1}$.

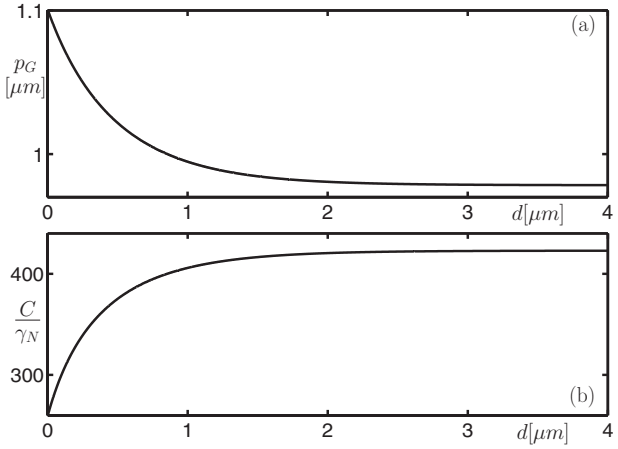

FIG. 11. Inverse coupling length p_G (a) and coupling rate C (b) as a function of the laser half distance d, as calculated from the transcendental equation (45) for $n_b = 3.61$, $w = 4.0$ μm, and $n_G = 3.6$.

Figure 11 shows the dependence of the inverse coupling length p_G and normalized coupling rate C/γ_N on the half distance d between the lasers as calculated from Eqs. (45) and (48). Clearly, for sufficiently weak coupling (large half distance d) each of these parameters can be approximated by a constant as is commonly done in the weak-coupling theory with $C/\gamma_N \approx 420$ and $p_G \approx 0.98 \times 10^6\ \mathrm{m}^{-1}$. However, for strong coupling (small d), C and p_G vary noticeably with d.

Using the simplified model (12) for the polarization $P_{A,B}$ of the semiconductor active medium in Eqs. (46) and rescaling time and variables (Appendix A) one arrives at the coupled-laser model:

$$\frac{d\tilde{E}_{A,B}}{d\tilde{t}} = -i(\tilde{\Omega}_{A,B} - \tilde{\nu})\tilde{E}_{A,B} + (1 - i\alpha)\beta\gamma\tilde{N}_{A,B}\tilde{E}_{A,B} + i\kappa E_{B,A},$$

$$\frac{d\tilde{N}_{A,B}}{d\tilde{t}} = \tilde{\Lambda} - (\tilde{N}_{A,B} + 1) - (1 + \beta\tilde{N}_{A,B})|\tilde{E}_{A,B}|^2, \tag{49}$$

where $\tilde{\Omega}_{A,B} = (\Omega'_{A,B} - C)/\gamma_N$ and the coupling parameter

$$\kappa = \frac{C}{\gamma_N}\exp(-2dp_G). \tag{50}$$

Equations (49) govern the time evolution of the normalized complex-valued electric fields $\tilde{E}_{A,B}(\tilde{t})$ and the normalized carrier densities $\tilde{N}_{A,B}(\tilde{t})$ of lasers A and B. In the remainder of this section we again drop the tildes for the rescaled quantities for convenience. Equations (49) are very similar to the individual-laser model (31) but differ by a factor $i = \exp(i\pi/2)$ in the coupling term. In physical terms, this is

merely a $\pi/2$ phase shift in the phase of the coupling field. However, mathematically, the coupled-laser equations are not invariant under such a phase-shift transformation and, hence, the coupled-laser model has different solutions as we will show in the next section.

Weak-coupling theory was used first by Spencer and Lamb in Refs. [1,2], who derived a coupled-laser model for face-to-face coupling that also contains the imaginary unit i in the coupling terms. A similar model was then proposed and used by Wang and Winful in Refs. [66,67] to study nonlinear dynamics and synchronization in side-to-side coupled semiconductor lasers. Their model has also been used (although less extensively than the individual-laser model) by other investigators, for example, in Refs. [14,68–72]. The derivation in this section verifies that coupled-laser model (49) is a valid approximation of the wave equation (1) for (weakly) side-to-side coupled semiconductor lasers.

D. Dynamics of the coupled-laser model

Unlike the individual-laser model (31), the coupled-laser model (49) does not have cw solutions with identical laser amplitudes for $\Delta\Omega=\Omega_A-\Omega_B\neq 0$. Instead, the cw solutions are of the form

$$E_A(t)=|E_A^0|e^{-i\omega^0 t},\quad N_A(t)=N_A^0,$$

$$E_B(t)=|E_B^0|e^{-i\omega^0 t-i\varphi},\quad N_B(t)=N_B^0. \tag{51}$$

The situation when $|E_A^0|=|E_B^0|$ is a special case that occurs only for $\Delta\Omega=0$.

A bifurcations analysis of the coupled-laser model (49) is presented in Figs. 12 and 13 for three different, representative values of α. The comparison with the bifurcation structure of the composite-cavity model (27) in Figs. 7(a), 7(c), 7(f), and 8 shows a very good agreement in weak-coupling conditions, namely, for $d>1.5$ μm where p_G and C are approximately constant as shown in Fig. 11. Significant differences occur only in strong-coupling conditions for small d. In particular, the individual-laser model (49) fails to reproduce the different locking regions with one stable cw solution found in Fig. 7(a) for the composite-cavity model. Also, the bifurcation diagrams for $\alpha=0.4$ and 2 in Figs. 13(b) and 13(c) agree well with the results for the composite-cavity model in Figs. 8(b) and 8(c) for weak coupling. In particular, Eqs. (49) reproduce the gap in the locking region that is filled with bifurcations of periodic solutions and chaotic dynamics. Furthermore, we checked that the bifurcation diagrams in Fig. 13 for the coupled-laser model and Fig. 8 for the composite-cavity model undergo the same qualitative transitions when α is varied.

The weak-coupling models Eqs. (31) and (49) are quite general: as long as one does not specify the coupling parameter κ these models are independent of the actual coupling geometry, such as the side-to-side or face-to-face configuration. Therefore, it is interesting and straightforward to compare them for different coupling conditions. Clearly, the individual-laser model (31) and coupled-laser model (49) give rise to completely different bifurcation diagrams at weak- to moderate-coupling conditions. To further check

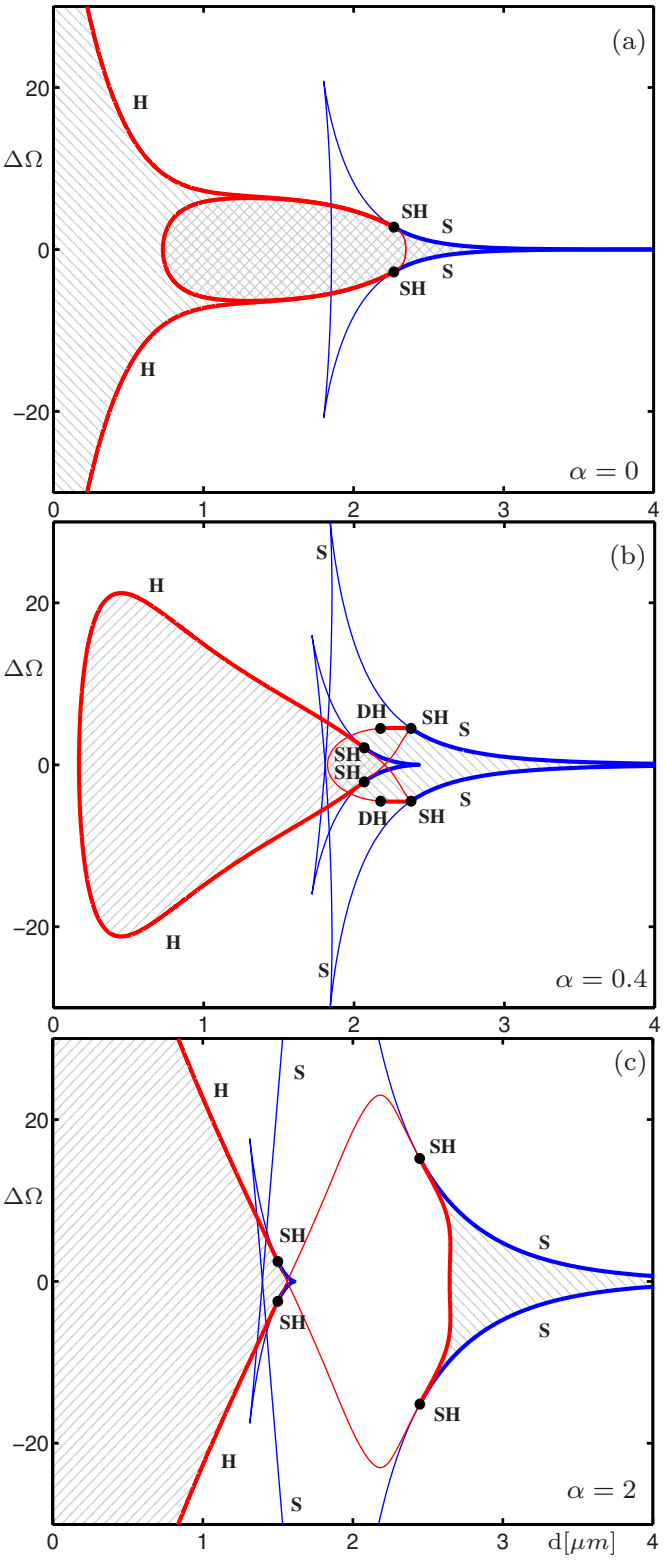

FIG. 12. (Color online) Two-parameter bifurcation diagram in the $(d,\Delta\Omega)$ plane of Eqs. (49) for $\alpha=0$ (a), 0.4 (b), and 2 (b), showing curves of saddle-node (S) and Hopf (H) bifurcations and codimension-2 saddle-node Hopf (SH), and degenerate Hopf (DH) points; the hatched regions indicate the stable cw solution.

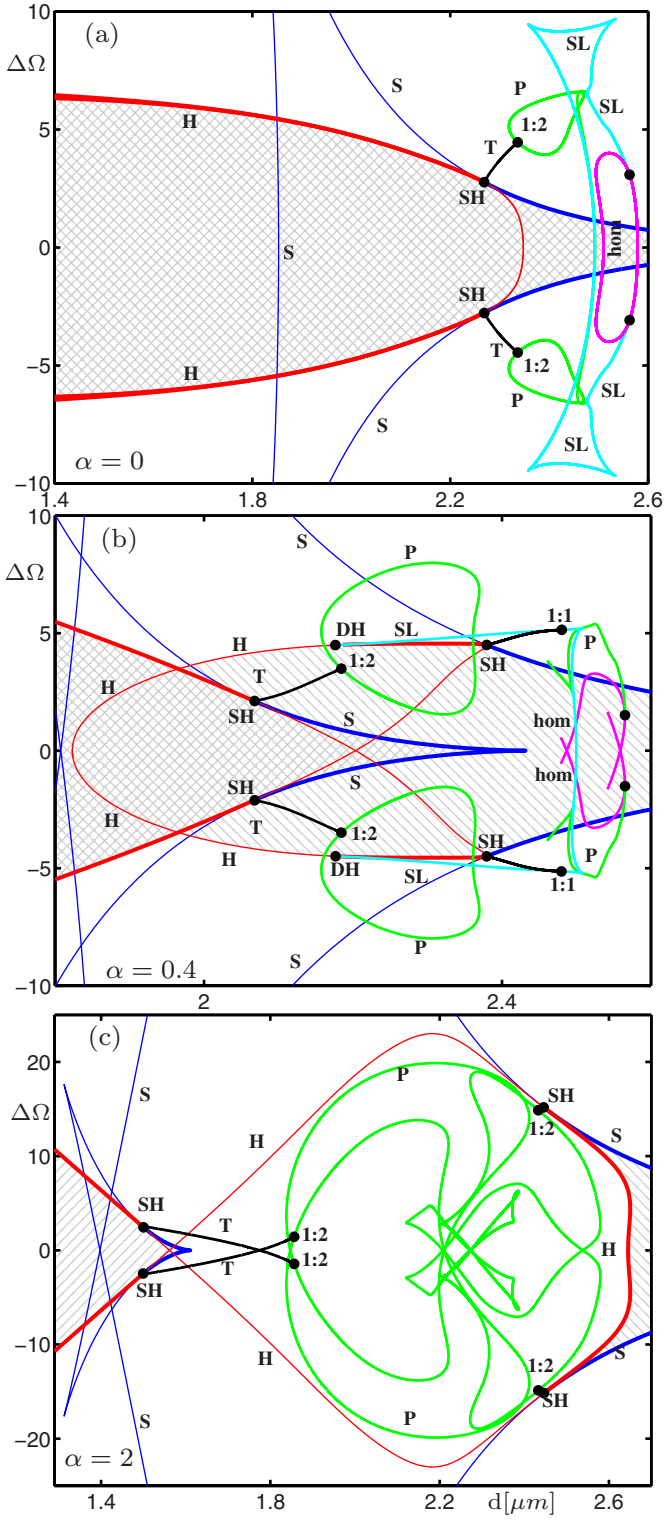

FIG. 13. (Color online) Two-parameter bifurcation diagram in the $(d,\Delta\Omega)$ plane of Eqs. (49) for α=0 (a), 0.4 (b), and 2 (b), also showing curves of period doubling (PD), torus (T), saddle-node (SL) of limit-cycle, and homoclinic (hom) bifurcations, and codimension-2 saddle-node Hopf (SH) 1:2-resonance (1:2) points; hatched regions indicate stable cw solution.

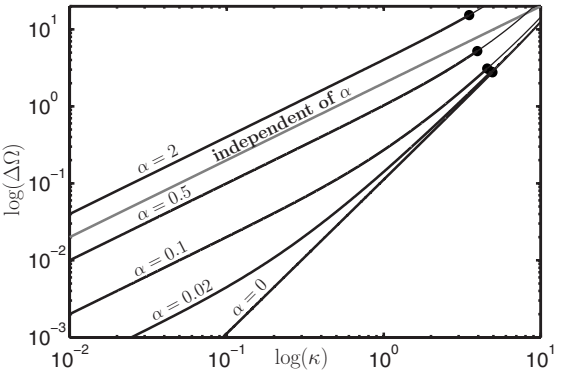

FIG. 14. Locking boundary in weak-coupling conditions given by the saddle-node bifurcation for different values of α in the individual-laser model (31) (gray) and the coupled-laser model (49) (black). The dots denote saddle-node Hopf points where the saddle-node curves change from super-to subcritical.

whether these weak-coupling models agree at least in the limit of vanishing coupling, Fig. 14 shows on a doubly logarithmic scale in the $(\kappa,\Delta\Omega)$ plane the curves of the locking-unlocking transition (as given by the saddle-node bifurcationcurves). Note that there are differences even in the limit of vanishing coupling. Whereas the scaling of the locking region is independent of the linewidth enhancement factor α in the individual-laser model (gray), it shows significant variations with α in the coupled-laser model (black).

V. CONCLUSIONS

In this paper we considered different modeling approaches for the study of the nonlinear dynamics of semiconductor lasers that are coupled side to side. For the case of two laterally coupled lasers we used bifurcation analysis to identify relevant dynamics in the plane of the laser distance (coupling strength) and cavity width difference (detuning) for different values of the linewidth enhancement factor. In this way, we uncovered and explained significant differences in the dynamics obtained from different models that are widely used in the field.

First, we derived a composite-cavity model for the side-to-side coupled-laser device. This model properly accounts for the coupling between different lasers by expanding the laser field in terms of eigenfunctions for the whole coupled-laser system and, hence, is valid for arbitrary coupling conditions. A composite-cavity model is quite complicated in that it consists of a set of ordinary differential equations that are subject to additional algebraic constraints (to define the composite-cavity modes). Nevertheless, in simple cases like the one considered here, the composite-cavity model is amenable to bifurcation analysis with numerical continuation. This allowed us to identify key features of the dynamics for any value of the distance between the two stripes, that is, over the entire range of coupling strengths. Under weak- to moderate-coupling conditions, we found bistability of the (continuous-wave) phase-locked solutions, saddle-node Hopf bifurcation points giving rise to complicated dynamics, as well as strong dependence of the locking region and instabilities on the linewidth enhancement factor. Under strong-

coupling conditions, we found single composite-mode operation owing to strong competition of the composite-cavity modes, which become the modes of a single laser of twice the width of the individual lasers when the distance between them approaches zero. The overall qualitative features of the side-to-side coupled lasers are quite similar to those of two face-to-face coupled lasers (as also modeled by a composite-cavity model) [20,37].

Furthermore, we considered simpler rate equation models. Our starting point was the analysis of an individual-laser model, where coupling between individual lasers is introduced phenomenologically. While this model has been widely used in the literature to describe a number of laser systems, we demonstrated that it does not reproduce any relevant aspects of the dynamics found in the composite-cavity model of two laterally coupled lasers. What is more, already for weak-coupling conditions we uncovered a singularity in the solution of the individual-laser model, such that the lasers' intensity becomes infinite. We found that the differences between the two models appear because the phenomenologically introduced coupling terms in the individual-laser model are not in agreement with the boundary conditions for the side-to-side coupled-laser configuration considered here, nor for the face-to-face coupled-laser configuration considered in Refs. [2,37]. For this reason, we used the semiclassical theory of coupled lasers from Ref. [1] to derive a third model, called here the coupled-laser model, with coupling terms that are consistent with the solution of the wave equation and the appropriate boundary conditions. While this coupled-laser model has been introduced and used before [14,66–72], our calculations verified its validity for the case of side-to-side coupled lasers. Specifically, we showed by a bifurcation study that the coupled-laser model captures all the relevant dynamics found in the composite-cavity model, provided the coupling is not too strong. Finally, we mention that some investigators [65] use the phase of the coupling terms as a free parameter. The results based on weak-coupling theory for side-to-side and face-to-face coupled lasers showed that there is just one value for the phase that satisfies the corresponding boundary conditions.

While this work considers a specific side-to-side coupled-laser system, the results provide general insight into modeling and instabilities of coupled lasers. Composite-cavity models are an attractive class of models, because they describe the dynamics accurately over the entire range of coupling strengths while still allowing for detailed studies of the dynamics and bifurcations. However, when one is not interested in strong coupling, or when the array consists of many lasers, then simpler rate equation models are highly desirable. For example, coupled-laser models such as Eqs. (49) emerge as promising candidates for the study of nonlinear dynamics in large two-dimensional arrays composed of nonidentical (semiconductor) lasers.

ACKNOWLEDGMENTS

This research was supported by Great Western Research Grant No. 18 "Modelling and Nonlinear Dynamics of Optical Nanodevices: Nanolasers and Photonic Nanocircuits."

APPENDIX A: SCALING

Equations (27) for the composite-cavity model, Eqs. (31) for the individual-laser model, and Eqs. (49) for the coupled-laser model are written in dimensionless form; see also Ref. [37] for details. Here we denote the dimensionless quantities with a tilde. Specifically, time t is in units of the inverse population decay rate γ_N,

$$\tilde{t} = t\gamma_N. \tag{A1}$$

The carrier density is given with respect to the carrier density N_{thr} at threshold,

$$\tilde{N} = \frac{N - N_{\text{thr}}}{N_{\text{thr}}}, \tag{A2}$$

and the electric field amplitude is given with respect to its solitary-laser value at twice the threshold value:

$$|\tilde{E}| = |E|\left(\frac{2\hbar\nu\Gamma\gamma_N N_{\text{thr}}}{\epsilon_0 n_b^2 \gamma_E}\right)^{-1/2}. \tag{A3}$$

Furthermore, the dimensionless parameters are given as

$$\tilde{\Omega}_k = \frac{\Omega_k}{\gamma_N},$$

$$\gamma = \frac{\gamma_E}{2\gamma_N},$$

$$\beta = 1 + \frac{2c\Gamma\xi N_{ts}}{n_b\gamma_E},$$

$$\tilde{\Lambda} = \frac{\Lambda}{\gamma_N N_{\text{thr}}}, \tag{A4}$$

The local gain at threshold is given by

$$g_{\text{thr}} = \frac{n_b\gamma_E}{2c\Gamma}, \tag{A5}$$

and the population density at threshold, N_{thr}, is

$$N_{\text{thr}} = N_{ts} + \frac{n_b\gamma_E}{2c\Gamma\xi}, \tag{A6}$$

where N_{ts} is the population density at transparency. Parameter values in physical units can be found in Table I.

APPENDIX B: POLAR COORDINATES

For convenience, we rewrite here the rate equation models in polar coordinates $|E_n(t)|$ and $\Phi_n(t)$ with $E_n(t) = |E_n(t)|\exp[-i\Phi_n(t)]$.

The composite-cavity model, Eqs. (27), in polar coordinates reads

$$\frac{d|E_j|}{dt} = -\gamma|E_j| + \gamma K_{jj}\sum_{j'}\left(\sum_s [K^s_{j'j}(1+\beta N_s)\cos(\Phi_{j'j}) - \beta K^s_{j'j}\alpha^s(1+N_s)\sin(\Phi_{j'j})]\right)|E'_j|,$$

TABLE I. Laser parameters and their values.

Symbol	Meaning	Value
α	Linewidth enhancement factor	$0 \leqslant \alpha \leqslant 2$
γ_E	Cavity decay rate	1×10^{11} s^{-1}
γ_N	Carrier decay rate	5×10^{9} s^{-1}
ξ	Differential gain	2.22×10^{-20} m^2
Γ	Confinement factor	0.1
N_{ts}	Carrier density at transparency	2.0×10^{24} m^{-3}
n_b	Background refractive index	3.6
N_{thr}	Carrier density at threshold	
ϵ_0	Dielectric constant of vacuum	
c	Speed of light in vacuum	
$\hbar$	Planck's constant divided by 2π	

$$\frac{d\Phi_j}{dt} = \Omega_j - \nu_j + \gamma K_{jj} \sum_{j'} \left(\sum_s [\beta K^s_{j'j} \alpha^s (1 + N_j) \cos(\Phi_{j'j}) + \beta K^s_{j'j} (1 + \beta N_s) \sin(\Phi_{j'j})] \right) \frac{|E_{j'}|}{|E_j|},$$

$$\frac{dN_s}{dt} = \Lambda_s - (N_s + 1) - \sum_{j',j} K^s_{j'j} (1 + \beta N_s) \cos(\Phi_{j'j}) |E_{j'}||E_j|. \tag{B1}$$

In these equations the subscript j denotes the composite-cavity modes, s the laser active stripes, and $\Phi_{jj'} = \Phi_j - \Phi_{j'}$ the time-dependent phase difference between two composite-cavity modes j and j'.

The individual-laser model, Eqs. (31), in polar coordinates reads

$$\frac{d|E_n|}{dt} = \beta\gamma N_n |E_n| + \sum_{k \neq n} \kappa \cos \Phi_{kn} |E_k|,$$

$$\frac{d\Phi_{kn}}{dt} = \Delta\Omega_{kn} + \alpha\beta\gamma(N_k - N_n) - \sum_{k \neq n} \kappa \left(\frac{|E_n|^2 + |E_k|^2}{|E_k||E_n|} \right) \sin \Phi_{kn} |E_k|,$$

$$\frac{dN_n}{dt} = \Lambda - (N_n + 1) - (1 + \beta N_n)|E_n|^2. \tag{B2}$$

The coupled-laser model, Eqs. (49), in polar coordinates reads

$$\frac{d|E_n|}{dt} = \beta\gamma N_n |E_n| + \sum_{k \neq n} \kappa \sin \Phi_{kn} |E_k|,$$

$$\frac{d\Phi_{kn}}{dt} = \Delta\Omega_{kn} + \alpha\beta\gamma(N_k - N_n) - \sum_{k \neq n} \kappa \left(\frac{|E_n|^2 + |E_k|^2}{|E_k||E_n|} \right) \cos \Phi_{kn} |E_k|,$$

$$\frac{dN_n}{dt} = \Lambda - (N_n + 1) - (1 + \beta N_n)|E_n|^2. \tag{B3}$$

In Eqs. (B2) and (B3) the subscripts k,n denote the two lasers A and B, and we have introduced the detuning $\Delta\Omega_{kn} = \Omega_k - \Omega_n$ and the phase difference $\Phi_{kn} = \Phi_k - \Phi_n$.

[1] M. Spencer and J. W. E. Lamb, Phys. Rev. A **5**, 884 (1972).
[2] M. Spencer and J. W. E. Lamb, Phys. Rev. A **5**, 893 (1972).
[3] *Diode Laser Arrays*, edited by D. Botez and D. Scifres (Cambridge University Press, Cambridge, U.K., 1994).
[4] M. Möhrle, B. Sartorius, C. Bornholdt, S. Bauer, O. Brox, A. Sigmund, R. Steingrüber, M. Radziunas, and H.-J. Wünsche, IEEE J. Sel. Top. Quantum Electron. **7**, 217 (2001).
[5] W. W. Chow, J. Opt. Soc. Am. B **3**, 833 (1986).
[6] A. Uchida, R. McAllister, R. Meucci, and R. Roy, Phys. Rev. Lett. **91**, 174101 (2003).
[7] A. Uchida, F. Rogister, and R. R. J. García-Ojalvo, Prog. Opt. **48**, 203 (2005).
[8] W. Fader, IEEE J. Quantum Electron. **QE-21**, 1838 (1985).
[9] D. J. DeShazer, R. Breban, E. Ott, and R. Roy, Phys. Rev. Lett. **87**, 044101 (2001).
[10] P. Ashwin, G. Orosz, J. Wordsworth, and S. Townley, SIAM J. Appl. Dyn. Syst. **6**, 728 (2007).
[11] O. E. Omel'chenko, Y. L. Maistrenko, and P. A. Tass, Phys. Rev. Lett. **100**, 044105 (2008).
[12] S. Yanchuk, A. Stefanski, T. Kapitaniak, and J. Wojewoda, Phys. Rev. E **73**, 016209 (2006).
[13] J. R. Terry, K. S. Thornburg, Jr., D. J. DeShazer, G. D. VanWiggeren, S. Zhu, P. Ashwin, and R. Roy, Phys. Rev. E **59**, 4036 (1999).
[14] P. Mandel, Li Ruo-ding, and T. Erneux, Phys. Rev. A **39**, 2502 (1989).
[15] J. García-Ojalvo, T. M. C., and V. R., Quantum Semiclassic. Opt. **10**, 809 (1998).
[16] J. García-Ojalvo, M. Brambilla, M. C. Torrent, and R. Vilaseca, Chaos, Solitons Fractals **10**, 819 (1999).
[17] J. Mulet, C. Mirasso, T. Heil, and I. Fischer, J. Opt. B: Quantum Semiclassical Opt. **6**, 97 (2004).
[18] J. Mulet, C. Masoller, and C. R. Mirasso, Phys. Rev. A **65**, 063815 (2002).
[19] H. Erzgräber, D. Lenstra, B. Krauskopf, E. Wille, M. Peil, I. Fischer, and W. Elsäßer, Opt. Commun. **255**, 286 (2005).
[20] S. Wieczorek and W. W. Chow, Phys. Rev. A **69**, 033811 (2004).
[21] S. A. Shakir and W. W. Chow, Opt. Lett. **9**, 202 (1984).
[22] S. A. Shakir and W. W. Chow, Phys. Rev. A **32**, 983 (1985).
[23] E. Kapon and J. Katz, Opt. Lett. **9**, 125 (1984).
[24] C. R. Mirasso, M. Kolesik, M. Matus, J. K. White, and J. V. Moloney, Phys. Rev. A **65**, 013805 (2001).
[25] O Hess, in *Fundamental Issues of Nonlinear Laser Dynamics*,

edited by B. Krauskopf and D. Lenstra, AIP Conf. Proc. No. 548 (AIP, Melville, NY, 2000), pp. 128–148.
[26] M. Matus, J. V. Moloney, and M. Kolesik, Phys. Rev. E **67**, 016208 (2003).
[27] M. Radziunas and H. J. Wünsche, in *Optoelectronic Devices—Advanced Simulation and Analysis*, edited by J. Piprek (Springer, New York, 2004).
[28] S. Riyopoulos, Phys. Rev. A **66**, 053820 (2002).
[29] P. Debernardi, G. P. Bava, F. Monti di Sopra, and M. Willemsen, IEEE J. Quantum Electron. **QE-39**, 109 (2003).
[30] A. G. Vladimirov, G. Kozyreff, and P. Mandel, Europhys. Lett. **61**, 613 (2003).
[31] F. Rogister, K. S. Thornburg, L. Fabiny, M. Moller, and R. Roy, Phys. Rev. Lett. **92**, 093905 (2004).
[32] S. Riyopoulos, Chaos **14**, 1105 (2004).
[33] B. Pasenow, M. Reichelt, T. Stroucken, T. Meier, S. W. Koch, A. R. Zakharian, and J. V. Moloney, J. Opt. Soc. Am. B **22**, 2039 (2005).
[34] J. J. Raftery, Jr., A. J. Danner, J. C. Lee, and K. D. Choquette, Appl. Phys. Lett. **86**, 201104 (2005).
[35] W. W. Chow, J. Opt. Soc. Am. B **4**, 324 (1987).
[36] S. Wieczorek and W. W. Chow, Phys. Rev. Lett. **92**, 213901 (2004).
[37] S. Wieczorek and W. W. Chow, Opt. Commun. **246**, 471 (2005).
[38] K. S. Thornburg, M. Möller, R. Roy, T. W. Carr, R.-D. Li, and T. Erneux, Phys. Rev. E **55**, 3865 (1997).
[39] L. Fabiny, P. Colet, R. Roy, and D. Lenstra, Phys. Rev. A **47**, 4287 (1993).
[40] Y. Braiman, T. A. B. Kennedy, K. Wiesenfeld, and A. Khibnik, Phys. Rev. A **52**, 1500 (1995).
[41] P. Ashwin, J. R. Terry, K. S. Thornburg, and R. Roy, Phys. Rev. E **58**, 7186 (1998).
[42] A. I. Khibnik, Y. Braiman, T. A. B. Kennedy, and K. Wiesenfeld, Physica D **111**, 295 (1998).
[43] A. I. Khibnik, Y. Braiman, V. Protopopescu, T. A. B. Kennedy, and K. Wiesenfeld, Phys. Rev. A **62**, 063815 (2000).
[44] R. A. Oliva and S. H. Strogatz, Int. J. Bifurcation Chaos Appl. Sci. Eng. **11**, 2359 (2001).
[45] H. G. Winful, S. Allen, and L. Rahman, Opt. Lett. **18**, 1810 (1993).
[46] J. E. Carroll and I. H. White, Philos. Trans. R. Soc. London, Ser. A **313**, 333 (1984).
[47] O. Hess and E. Schöll, Physica D **70**, 165 (1994).
[48] O. Hess and E. Schöll, Phys. Rev. A **50**, 787 (1994).
[49] D. Merbach, O. Hess, H. Herzel, and E. Schöll, Phys. Rev. E **52**, 1571 (1995).
[50] H. Lamela, M. Leones, G. Carpintero, C. Simmendinger, and O. Hess, IEEE J. Sel. Top. Quantum Electron. **7**, 192 (2001).
[51] M. Yousefi, A. Barsella, D. Lenstra, G. Morthier, R. Baets, S. McMurtry, and J. Vilcot, IEEE J. Quantum Electron. **QE-39**, 1229 (2003).
[52] G. Carpintero, H. Lamela, M. Leonés, C. Simmendinger, and O. Hess, Appl. Phys. Lett. **78**, 4097 (2001).
[53] H. Lamela, M. Leonés, G. Carpintero, C. Simmendinger, and O. Hess, IEEE J. Sel. Top. Quantum Electron. **7**, 192 (2001).
[54] H. Lamela, B. Roycroft, P. Acedo, R. Santos, and G. Carpintero, Opt. Lett. **27**, 303 (2002).
[55] P. Acedo, H. Lamela, B. Roycroft, G. Carpintero, and R. Santos, IEEE Photonics Technol. Lett. **14**, 1055 (2002).
[56] M. Sargent III, M. Scully, and W. Lamb, *Laser Physics* (Addison-Wesley, New York, 1974).
[57] W. Chow, S. Koch, and M. Sargent III, *Semiconductor Laser Physics* (Springer Verlag, Berlin, 1997).
[58] W. Chow and S. Koch, *Semiconductor-Laser Fundamentals* (Springer-Verlag, Berlin, 1999).
[59] W. W. Chow, IEEE J. Quantum Electron. **QE-22**, 1174 (1986).
[60] E. Doedel, A. Champneys, T. Fairgieve, Y. Kuznetsov, B. Oldeman, R. Paffenroth, B. Sandstede, X. Wang, and C. Zhang, Concordia University, technical report, Montreal, Canada, 2007 (unpublished).
[61] *Numerical Continuation Methods for Dynamical Systems: Path Following and Boundary Value Problems*, edited by B. Krauskopf, H. Osinga, and J. Galán-Vioque (Springer-Verlag, Berlin, 2007).
[62] S. Wieczorek, B. Krauskopf, and D. Lenstra, Opt. Commun. **172**, 279 (1999).
[63] Y. Kuznetsov, *Elements of Applied Bifurcation Thory* (Springer-Verlag, Berlin, 2004).
[64] J. Guckenheimer and P. Holmes, *Nonlinear Oscillations, Dynamical Systems, and Bifurcations of Vector Fields* (Springer-Verlag, Berlin, 1983).
[65] S. Yanchuk, K. R. Schneider, and L. Recke, Phys. Rev. E **69**, 056221 (2004).
[66] H. G. Winful, Phys. Rev. A **46**, 6093 (1992).
[67] S. S. Wang and H. G. Winful, Appl. Phys. Lett. **52**, 1774 (1988).
[68] R. Li and T. Erneux, Opt. Commun. **99**, 196 (1993).
[69] R. D. Li and T. Erneux, Phys. Rev. A **49**, 1301 (1994).
[70] H. G. Winful and S. S. Wang, Appl. Phys. Lett. **53**, 1894 (1988).
[71] H. G. Winful and L. Rahman, Phys. Rev. Lett. **65**, 1575 (1990).
[72] K. Otsuka, Phys. Rev. Lett. **65**, 329 (1990).